BRNO UNIVERSITY OF TECHNOLOGY
VYSOKÉ UČENÍ TECHNICKÉ V BRNĚ

FACULTY OF MECHANICAL ENGINEERING
FAKULTA STROJNÍHO INŽENÝRSTVÍ

INSTITUTE OF PHYSICAL ENGINEERING
ÚSTAV FYZIKÁLNÍHO INŽENÝRSTVÍ

SIMULATIONS OF LIGHT SCATTERING FROM LIVING CELLS
SIMULACE ROZPTYLU SVĚTLA NA BUŇKÁCH

MASTER'S THESIS
DIPLOMOVÁ PRÁCE

AUTHOR — **Bc. Martin Vengh**
AUTOR PRÁCE

SUPERVISOR — **prof. RNDr. Jiří Petráček, Dr.**
VEDOUCÍ PRÁCE

BRNO 2018

VYSOKÉ UČENÍ TECHNICKÉ V BRNĚ
FAKULTA STROJNÍHO INŽENÝRSTVÍ

Zadání diplomové práce

Ústav:	Ústav fyzikálního inženýrství
Student:	**Bc. Martin Vengh**
Studijní program:	Aplikované vědy v inženýrství
Studijní obor:	Přesná mechanika a optika
Vedoucí práce:	**prof. RNDr. Jiří Petráček, Dr.**
Akademický rok:	2017/18

Ředitel ústavu Vám v souladu se zákonem č.111/1998 o vysokých školách a se Studijním a zkušebním řádem VUT v Brně určuje následující téma diplomové práce:

Simulace rozptylu světla na buňkách

Stručná charakteristika problematiky úkolu:

Informace získané pomocí rozptylu světla na buňkách mohou posloužit k rychlé a neinvazivní diagnostice biologických tkání. Příkladem mohou být metody holografické mikroskopie umožňující kvantitativní zobrazování živých buněk bez použití kontrastních látek. Při vývoji těchto technik je nutné využívat numerické simulace založené na teorii rozptylu (Bornova a Rytovova aproximace) nebo na rigorózním řešení Maxwellových rovnic v nehomogenním prostředí (metoda konečných diferencí v časové oblasti). Práce se zaměří na výběr způsobu výpočtu rozptylu světla, který bude prakticky využitelný při výzkumu metod holografické mikroskopie.

Cíle diplomové práce:

1. Rešeršní studie zaměřená na praktické způsoby výpočtu rozptylu světla na buňkách.
2. Výběr vhodné metody využitelné při výzkumu nekoherentní holografické mikroskopie.
3. Porovnání vybrané metody s rigorózní metodou konečných diferencí v časové oblasti pomocí simulací rozptylu světla na vhodném modelu buňky.

Seznam doporučené literatury:

TANEV, S. et al. FDTD Simulation of Light Interaction with Cells for Nanobiophotonics Diagnostics and Imaging. In: Handbook of Photonics for Biomedical Science (Tuchin, Valery ed.). Boca Raton: CRC Press, 2010, s. 3-45.

KARLSSON, A. et al. Numerical Simulations of Light Scattering by Red Blood Cells. IEEE Transactions on Biomedical Engineering. 2005, 52(1), 13–18.

LIM, J. et al. Born Approximation Model for Light Scattering by Red Blood Cells. Biomedical Optics Express. 2011, 2(10), 2784–91.

LIM, J. et al. Born Approximation Model for Light Scattering by Red Blood Cells. Biomedical Optics Express. 2011, 2(10), 2784–91.

SUNG, Y. et al. Optical Diffraction Tomography for High Resolution Live Cell Imaging. Optics Express. 2009, 17(1), 266–77.

Students are required to submit the thesis within the deadlines stated in the schedule of the academic year 2017/18.

In Brno, 1. 11. 2017

VYSOKÉ UČENÍ TECHNICKÉ V BRNĚ
FAKULTA STROJNÍHO INŽENÝRSTVÍ
DĚKANÁT
L. S.

prof. RNDr. Tomáš Šikola, CSc.
Director of the Institute

doc. Ing. Jaroslav Katolický, Ph.D.
FME dean

Abstrakt

Diplomová práca sa zaoberá rozptylom elektromagnetického žiarenia na biologickej bunke použitím metódy konečných diferencií v časovej oblasti (FDTD), Bornovej aproximácie a Rytovovej aproximácie. Metóda FDTD dáva presné výsledky v širokej škále problémov. Je spravené porovnanie Bornovej aproximácie a Rytovovej aproximácie prostredníctvom FDTD metódy. Ďaľšia časť práce zahrnuje krátky popis koherenciou riadeného holografického mikroskopu CCHM. Záverečná časť sa venuje zobrazeniu rozptýleného poľa získaného z jednotlivých simulácií pomocou simulácie objektového ramena mikroskopu CCHM.

Summary

The master's thesis deals with the scattering of electromagneticc waves from a living cell using the finite-difference time-domain method (FDTD), the Born approximation and the Rytov approximation. FDTD is full wave method that gives accurate results in wide variety of scattering problems. The comparison of the Born aproximation and the Rytov aproximation is presented via FDTD method. Next part of my thesis includes a short description of coherence-controlled holographic microscope (CCHM). The final part deals with the imaging of the scattered field via simulation of object arm of CCHM, using results of the Born approximation, Rytov approximation and FDTD method.

Klíčová slova

Bornova aproximácia, Rytovova aproximácia, metoda konečných diferencií v časovej oblasti, holografická mikroskopia

Keywords

Born approximation, Rytov approximation, finite-difference time-domain, holographic microscopy

VENGH, M. *Přesná mechanika a optika.* Brno: Vysoké učení technické v Brně, Fakulta strojního inženýrství, 2018. 53 s. Vedoucí práce prof. RNDr. Jiří Petráček, Dr.

I hereby declare that I have written my master's thesis on the theme of *Simulations of light scattering from living cells* independently, under the guidance of the master's thesis supervisor, prof. RNDr. Jiří Petráček, Dr., and using the technical literature and other sources of information which are all properly quoted in the thesis and detailed in the list of literature at the end of the thesis.

Bc. Martin Vengh

I would like to thank prof. RNDr. Jiří Petráček, Dr., for his expert advice, encouragement and patience throughout this project. Also, I would like to thank my colleagues for their wonderful collabortion. You supported me greatly and were always willing to help me. Finally, I thank and I owe gratitude to my whole family for their support during my whole life.

Bc. Martin Vengh

Contents

Introduction

The nature of light provides wide variety of phenomena. Probably the most common is scattering with different areas of applications. Light scattering can be used as non-invasive process in imaging techniques. This makes light scattering highly applicable in biology. In this way, there is a present need of understanding the interaction of light with biological structures as tissues and cells. This may help to detect morphological changes in a tissue caused by disease, which can cause changes in scattered light. But it is difficult to meaningfully relate measurements to specific underlying physical changes. Thus, there is a need of quantitative model for simulating the scattering of structures of various shape to be able to make predictions of how effectively a particular optical diagnostic technique will be to detect disease.

This gives rise to various special imaging techniques. From direct methods, it can be confocal microscopy [1] or optical coherence tomography [2]. Among indirect methods, diffuse optical tomography is perhaps the best example of using measurement of light propagation in tissue to reconstruct tissue features that cannot otherwise be imaged and relies on reconstructing tissue properties based on transport theory due to multiple scattering [3, 4].

Clearly methods of modeling the scattering are needed and can help in development of new microscopy techniques.

1. Scattering

Scattering is a general physical process, where some forms of radiation, such as light, sound, or moving particles, are forced to deviate from a straight trajectory by one or more paths due to localized non-uniformities in the medium through which they pass. A passing through any inhomogeneous medium includes optical phenomenon such as law of refraction, reflection or diffraction. But it is rather hard to precisely define differences between phenomena as diffraction, scattering and interference. One may see a comparison in [5].

Scattering theory tries to mathematically describe scattering phenomenon. In general, the scattering may be divided into two major parts: elastic scattering and inelastic scattering. Inelastic scattering is process in which the kinetic energy of a incident particle is not conserved. It means that some of the energy is lost or increased. Examples of such scattering are Stokes and Anti-Stokes Raman scattering, which provide a structural fingerprint by which molecules can be identified. Another is Compton scattering, which is used, for instance, in radiation therapy. There are also many others types of inelastic scatterings with wide variety of usage in many applications areas. On the other hand, elastic scattering is process in which the kinetic energy of incident particle is conserved. Speaking in terms of electromagnetic scattering, we say that the wavelength of scattered wave is unchanged. Typical examples of elastic scattering are Rayleigh and Mie scattering. These examples describe scattering on small spherical particles. We can see in the Fig. (1.1) transitions among particular types of scattering depending on size r of a particle and wavelength λ, where $x = 2\pi r/\lambda$.

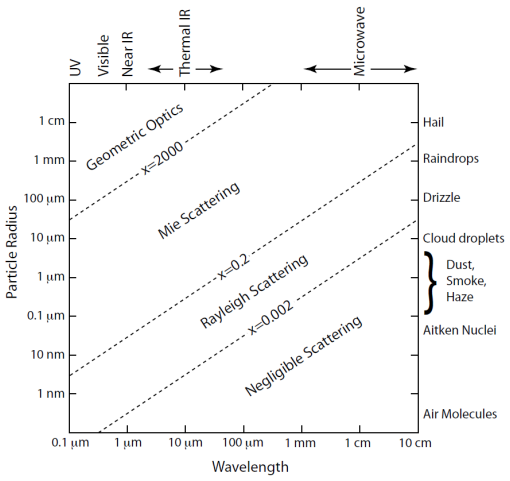

Figure 1.1: Scattering regimes on spherical particles [6].

Rayleigh and Mie scattering are obtained as analytical solutions of Maxwell's equations. Both methods are used to describe scattering on particles present, for instance in the atmosphere. Rayleigh scattering is used in description of wave scattering on molecules of air, whereas Mie scattering takes place where size of particles is about size of wavelength of light.

There are areas of applications, where scattering on objects with more complicated structures is present. For instance, it is biology, where object as tissues and cells do not exhibit any symmetry. In general, it is rather hard to describe scattering of such objects analytically. One have to simulate scattering via some approximative or rigorous numerical method. Then, these methods can be used in development of microscopy techniques.

1.1 Approximative methods

A number of different numerical methods have been applied in biology optics [7, 8, 9]. For instance, the T-matrix method which is a generalization of Mie scattering. The method is based on surface integral representation of the electric field and on expansions of the surface fields in sets of vector functions that are complete on the unit sphere. It was indicated, that the T-matrix method is not suitable method for simulating scattering on red blood cell with realistic shape [10]. Another one is the superposition approximation. The term superposition denotes that the scattering object is divided into several parts. Then the resulting scattered field is given as a sum of particular fields. This is based on the assumption that multiple scattering within the cell is small. Now, we introduce some other approximative methods, which belongs to more accurate methods for biological objects than reminded some above.

1.1.1 The discrete dipole approximation DDA

The discrete dipole approximation was proposed by Purcell and Pennypacker [11]. It is a general method to compute scattering and absorption of electromagnetic waves by particles of arbitrary geometry and composition. The scatterer is divided into a set of point dipoles. These dipoles interact with each other and the incident field, giving rise to a system of linear equations, which is solved to obtain dipole polarizations. All the measured scattering quantities can be obtained from these polarizations [12]. The total field is given by expression

$$E(\vec{r}_j) \quad = \quad \vec{E}(\vec{r}_j) + \sum_{k \neq j} \vec{A}(\vec{r}_j, \vec{r}_k)\vec{p}(\vec{r}_k), \tag{1.1}$$

where $\vec{A}(\vec{r}_j, \vec{r}_k)$ is the Green dyadic and $\vec{p}(\vec{r}_k)$ is a dipole moment. $\vec{r}_j$ is position of resulting electric field from a dipole at position $\vec{r}_k$. The light scattering by red blood cell [13] and particles much larger than the wavelength [14] was also simulated using DDA.

1.1.2 Born approximation BA

The Born approximation was first introduced by the German physicist Max Born in context of atomic particle scattering [15]. However it is also applicable to light scattering. The solution is obtained by the first order iteration of an integral equation for scattering problems. This means, that the total wave amplitude at a point is assumed to be equal to the amplitude of the incident wave. This is the mathematical expression of the assumption that only the primary scattered wave created by the incident wave is of importance, and every other scattering wave is neglected. Also this method was used in light scattering by red blood cells [16].

1.1.3 Rytov approximation RA

The Rytov approximation is widely used in line-of-sight propagation problems [17], also in problems of wave propagation in random media, diffraction tomography [18], or inverse-scattering theory [19]. It has the form of exponential representation. Also, the Rytov approximation may be expressed in terms of the first Born approximation. In some case it is considered to be superior to Born approximation.

1.2 Rigorous methods

Rigorous methods are considered as robust methods providing exact solutions and are applicable to wide range of scattering problems. Algorithms of rigorous methods are based on discretizing the whole domain into small parts of required dimension. The simulated problem is then computed in every node of simulation. There are various rigorous methods. Some of the most known are finite-difference time-domain (FDTD), pseudo-spectral time-domain (PSTD) and finite-element method (FEM). From names of methods we see, that FDTD and PSTD solve problem by discretizing space in time-domain, whereas FEM solves problem by discretizing space in frequency-domain. There are several available softwares based on these methods.

Advantages and disadvantages of rigorous methods

Rigorous methods provide several advantages to the problem. There is an option to define material and properties of structure in each point of simulation grid. As was mentioned these methods provide almost absolute accuracy. Also, some of them are simple and straightforward to implement. On the other hand, by rigorous methods we lose insight into the problem. Then, it is hard to tell which process plays major role in the problem. Also, the use of these methods is currently limited by computer resources. Thus, for particular problem an approximative method may be sufficient accurate and much faster.

1.3 Microscopy in biology

Microscopy in biology plays major role. It enables us to observe small object of various shapes. Most dominant type of light–cell interaction is elastic light scattering. Static light scattering originates from spatial heterogeneity of the optical refractive index. Spatially heterogeneous distribution of refractive index of various cell structures may affect light propagation including the spectroscopic, polarization, or angular features of scattered light emerging from tissue [20]. Biological cells are weakly absorbing and belong to phase objects (Fig. 1.2), mainly for wavelength in the near infrared [21]. This gives rise to microscopy techniques, where phase distortion of wave can be captured. Then, one speaks about the phase contrast microscopy. For instance, it is Zernike phase contrast microscopy [22], Differential interference contrast or Hoffman modulation-contrast microscopy [23]. Another technique is called holographic microscopy. We will discuss this technique in later chapter.

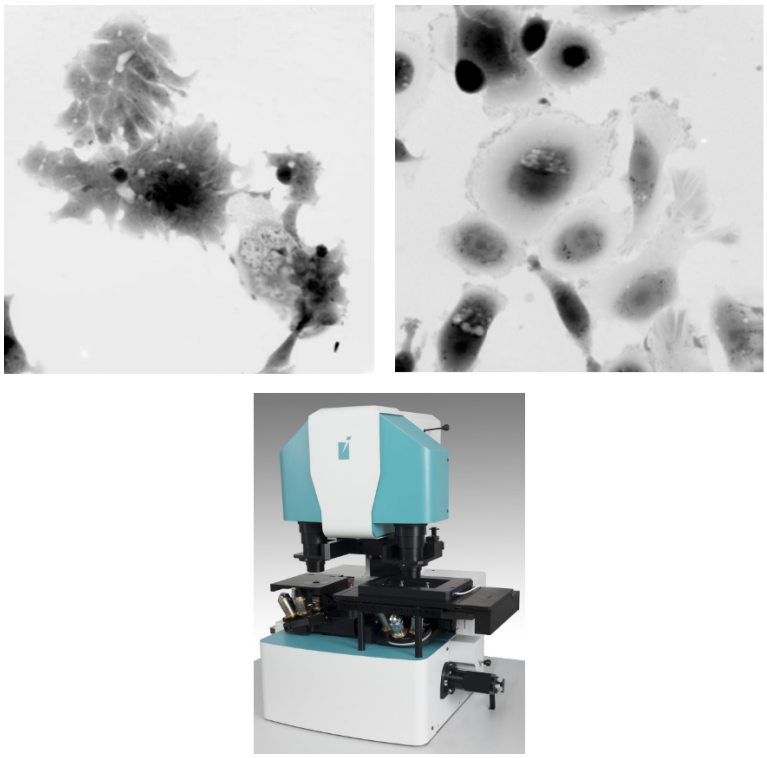

Figure 1.2: Illustrative images of phase objects and holographic microscopy [24].

2. Simulation methods

From approximative methods presented in the previous chapter, the Rytov and Born approximations were chosen. As will be seen later, it is because RA and RB require only one simulation and there have been done some work using RA and RB. From rigorous methods, it is the FDTD method. In this chapter, we mathematically define these approximations and consider its validity. Also, we introduce some basic concepts of simulations using FDTD. At the end of this chapter, we discuss parameters of the simulations and its results using approximative methods and rigorous method FDTD. First, we begin with Maxwell's equations and derivation of basic integral equation, which is necessary for derivation of BA, RA and FDTD method.

2.1 Maxwell's equations

Maxwell's equations fully describe macroscopic electromagnetic phenomena. According to system properties, Maxwell's equations can be simplified. For our purposes, the system is fully described with macroscopic quantity, index of refraction n. The Maxwell equations with no free charges and currents within studied system in MKS units are given by [25]

$$\nabla \times \vec{\mathcal{E}} = -\mu \frac{\partial \vec{\mathcal{H}}}{\partial t} \tag{2.1}$$

$$\nabla \times \vec{\mathcal{H}} = \epsilon \frac{\partial \vec{\mathcal{E}}}{\partial t} \tag{2.2}$$

$$\nabla \cdot \mu \vec{\mathcal{H}} = 0 \tag{2.3}$$

$$\nabla \cdot \epsilon \vec{\mathcal{E}} = 0, \tag{2.4}$$

where we used material equations

$$\vec{\mathcal{D}} = \epsilon \vec{\mathcal{E}} \tag{2.5}$$

$$\vec{\mathcal{B}} = \mu \vec{\mathcal{H}}, \tag{2.6}$$

where $\vec{\mathcal{D}}$ is electric displacement vector, $\vec{\mathcal{E}}$ is electric field and $\vec{\mathcal{H}}$ is magnetic field. μ and ϵ are the permeability and permittivity, respectively. ∇ is differential operator

such that $\nabla = (\frac{\partial}{\partial x}\vec{i}, \frac{\partial}{\partial y}\vec{j}, \frac{\partial}{\partial z}\vec{k})$. The symbols $\times$ and . represent a vector cross product and vector dot product, respectively.
Our interest is to obtain one differential equation describing system separately for each vector field. First, we divide both sides of the (2.1) by μ and apply operator $\nabla\times$. This gives

$$\nabla \times \left(\frac{1}{\mu}\nabla \times \vec{\mathcal{E}}\right) + \nabla \times \frac{\partial \vec{\mathcal{H}}}{\partial t} = 0. \tag{2.7}$$

Next we apply operator $\partial/\partial t$ to the first Maxwell equation (2.2), we have

$$\frac{\partial}{\partial t}\left(\nabla \times \vec{\mathcal{H}}\right) + \epsilon\frac{\partial^2 \vec{\mathcal{E}}}{\partial t^2} = 0. \tag{2.8}$$

Now, we change the order of space partial derivatives with time partial derivative in (2.7) thus, we eliminate the second term in (2.7) with the first term of (2.8). This gives

$$\nabla \times \left(\frac{1}{\mu}\nabla \times \vec{\mathcal{E}}\right) + \epsilon\frac{\partial^2 \vec{\mathcal{E}}}{\partial t^2} = 0. \tag{2.9}$$

Using identities (u represents $1/\mu$ and $\vec{v}$ represents $\nabla \times \vec{\mathcal{E}}$)

$$\nabla \times (u\vec{v}) = u[\nabla \times (\vec{v})] + \nabla(u) \times (\vec{v}) \tag{2.10}$$
$$\nabla \times \nabla\times = \nabla\nabla - \nabla^2 \tag{2.11}$$
$$\nabla(u\vec{v}) = u[\nabla(\vec{v})] + \nabla(u) \cdot \vec{v} \tag{2.12}$$

(2.9) becomes

$$\nabla^2\vec{\mathcal{E}}(\vec{r},\omega) + \epsilon\mu\frac{\partial^2 \vec{\mathcal{E}}}{\partial t^2} + \nabla ln\mu(\vec{r},\omega) \times \nabla \times \vec{\mathcal{E}} + \nabla[\vec{\mathcal{E}} \cdot \nabla ln\epsilon(\vec{r},\omega)] = 0. \tag{2.13}$$

This is initial equation for further analysis.

2.2 Cell as an inhomogenous medium

As was mentioned earlier, we are interested in simulations of light scattering from cell surrounded by homogeneous medium. In our further analysis we consider the response of the medium to the incident wave to be linear and is described by real macroscopic parameter(no absorption) - index of refraction $n(\vec{r},\omega)$. Next we assume that medium is time-independent, i.e. that at the macroscopic scale the physical properties do not change with time - static scattering, non-magnetic which means that magnetic permeability is equal to vacuum permeability μ_0. Moreover, we assume the medium to be non-dispersive, i.e. independent of wavelength $n(\vec{r},\omega) \to n(\vec{r})$ and isotropic, which means properties are independent of the direction of polarization of a wave.

2.3 Integral equation of scattering potential

Using stated assumptions and considering monochromatic electromagnetic field with time dependence $\exp(-i\omega t)$, without showing explicitly, (2.13) becomes [15]

$$\nabla^2\vec{\mathcal{E}}(\vec{r}) + k^2 n^2(\vec{r})\vec{\mathcal{E}} + \nabla[\vec{\mathcal{E}}(\vec{r}) \cdot \nabla ln\epsilon(\vec{r})] \quad = \quad 0, \tag{2.14}$$

where we used the assumption, that magnetic permeability is constant. Here

$$k \quad = \quad \frac{\omega}{c}. \tag{2.15}$$

It is rather hard to solve Eq. (2.14). The reason is that components of electric field become coupled, it is because in general, every component of $\nabla\epsilon(\vec{r})$ is dependent on each spatial coordinate. One can assume that the index of refraction is effectively constant over distances of the order of wavelength $\lambda = 2\pi/k$. This implies, that the last term of (2.14) may be neglected. Now, we have

$$\nabla^2\vec{\mathcal{E}}(\vec{r}) + k^2 n^2(\vec{r},\omega)\vec{\mathcal{E}}(\vec{r},\omega) \quad = \quad 0. \tag{2.16}$$

Cartesian component of $\vec{\mathcal{E}}$ are no longer coupled and together with medium isotropy, we can study the system for a single Cartesian component (which also neglects behavior on boundaries). This also brings a good insight into the behaviour of scattered field.

Denoting the component of $\vec{\mathcal{E}}$ by $U(\vec{r})$ we obtain the following scalar equation:

$$\nabla^2 U(\vec{r}) + k^2 n^2(\vec{r}) U(\vec{r}) \quad = \quad 0 \tag{2.17}$$

Many literatures rather re-write (2.17) to the form mathematically equivalent with the time-independent Schrödinger equation for non-relativistic particle. Thus, we obtain differential equation with non-zero right side

$$(\nabla^2 + k^2)U(\vec{r}) \quad = \quad -4\pi F(\vec{r},\omega)U(\vec{r}), \tag{2.18}$$

where

$$F(\vec{r},\omega) \quad = \quad \frac{1}{4\pi}k^2[n^2(\vec{r}) - 1]. \tag{2.19}$$

Function $F(\vec{r},\omega)$ is called scattering potential of the medium. It is the function defining object.

The fact, that Maxwell's equations are linear, and so is Helmholtz operator, it enables us to express the total field $U(\vec{r})$ as the sum of the incident field $U^i(\vec{r})$ and of the scattered field $U^s(\vec{r})$, as follows

$$U(\vec{r}) \quad = \quad U^i(\vec{r}) + U^s(\vec{r}). \tag{2.20}$$

For our purposes, as will be seen later, let incident field be a plane wave. Now, (2.17) becomes

$$(\nabla^2 + k^2)U^i(\vec{r}) + (\nabla^2 + k^2)U^s(\vec{r}) \quad = \quad -4\pi F(\vec{r},\omega)U(\vec{r}), \tag{2.21}$$

where

$$(\nabla^2 + k^2)U^i(\vec{r},\omega) \quad = \quad 0. \tag{2.22}$$

This is known as the Helmholtz equation and plane wave is one of its solutions. Using (2.22) we get

$$(\nabla^2 + k^2)U^s(\vec{r}) \quad = \quad -4\pi F(\vec{r},\omega)U(\vec{r}). \tag{2.23}$$

If it is possible, sometimes, it is more convenient to re-write differential equation into the form of an integral equation. Later, it enables us to make certain approximations.

One way to obtain such an integral equation is to use technique of Green's function. In mathematics, a Green's function is tool for solving inhomogeneous linear differential equations with specified initial and boundary conditions. Here, it is based on the fact of linearity of Helmholtz operator. Physically, it may be thought as the response of a system to a unit impulse at certain position $r = r'$. In other words, every point in domain is consider as a point source, described by Dirac delta function δ, giving rise to the spherical wave. Due to linearity, one can obtain solution by integrating throughout the whole domain. Speaking mathematically

$$(\nabla^2 + k^2)G(\vec{r} - \vec{r}') \quad = \quad -4\pi\delta^{(3)}(\vec{r} - \vec{r}'). \tag{2.24}$$

Combining (2.23) and (2.24) and applying Green's theorem (for particular steps see [15]), we obtain

$$U^s(\vec{r}) \quad = \quad \iiint_{-\infty}^{\infty} F(\vec{r},\omega)U(\vec{r})G(\vec{r} - \vec{r}')d^3r', \tag{2.25}$$

where Green's function [26]

$$G(\vec{r} - \vec{r}') \quad = \quad \frac{\exp(ik|\vec{r} - \vec{r}'|)}{|\vec{r} - \vec{r}'|}, \tag{2.26}$$

where $\vec{r}$ is position vector of observation and $\vec{r}'$ is the position vector of inhomogeneities, see (Fig. 2.1).

As we mentioned, incident field is a plane wave. Without loss of generality let $U^i(\vec{r})$ has amplitude of unity, frequency ω and direction of propagation denoted by wave vector $\vec{k}_0$.
For the total field $U(\vec{r})$ we have

$$U(\vec{r}) \quad = \quad \exp(i\vec{k}_0 \cdot \vec{r}) + \iiint_{-\infty}^{\infty} F(\vec{r}',\omega)U(\vec{r}')\frac{\exp[ik(\vec{r} - \vec{r}')]}{|\vec{r} - \vec{r}'|}d^3r'. \tag{2.27}$$

Eq. (2.27) is known as the integral equation of potential scattering and it is the basic equation for determining $U(\vec{r})$. It has the form of a iterative method. Each new calculated field has to be substituted into integral and re-calculated inside whole scattering volume. This means, that we calculate field only inside the scattering volume V. Once the solution throughout V is known, the solution outside V can be obtained by substituting into integral of (2.27).

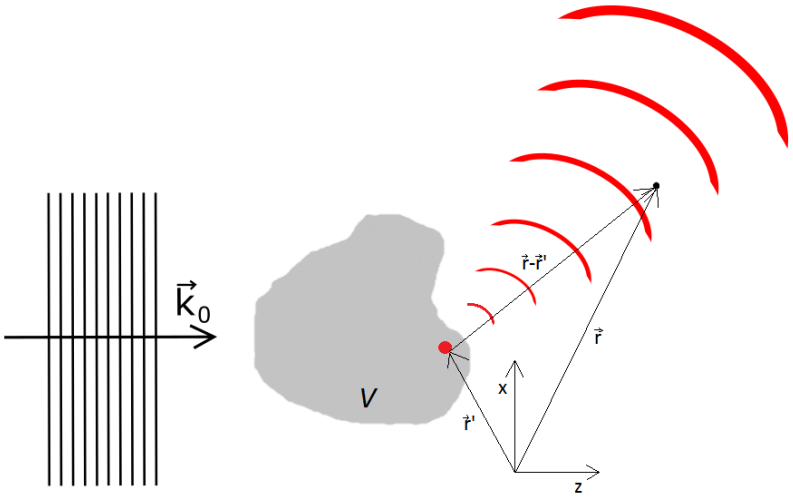

Figure 2.1: Illustrating the notation relating to scattering on a medium occupying a volume V.

2.4 First Born Approximation

In general, we don't know the field inside the scatterer, so one can make a first iteration, i.e. approximate field inside scatterer of equation (2.27). For slightly varying $n(\vec{r})$ from unity, let us replace the field $U(\vec{r}')$ inside the scatterer only by the incident field, mathematically

$$U \quad = \quad U^i + U^s \quad = \quad U^i. \tag{2.28}$$

This means that each point in the scatterer is affected only by incident field and no scattered field. One talks about single scattering. Moreover, we consider elastic scattering $|\vec{k}_0| = |\vec{k}\,'|$. Putting (2.28) into (2.27) we obtain

$$\begin{aligned} U(\vec{r}) \approx U_B(\vec{r}) \quad = \quad \exp(i\vec{k}_0 \cdot \vec{r}) + \iiint_{-\infty}^{\infty} F(\vec{r}',\omega) \exp(i\vec{k}_0 \cdot \vec{r}') \\ \times \frac{\exp[ik'(\vec{r}-\vec{r}')]}{|\vec{r}-\vec{r}'|} d^3r'. \end{aligned} \tag{2.29}$$

This approximation is generally referred to as the first Born approximation or just the Born approximation. In practice, one often measures a field far from the scatterer, so-called far field. Then for large r, it holds

$$|\vec{r}-\vec{r}'| \quad = \quad \sqrt{r^2 - 2\vec{r}.\vec{r}' + r'^2} \quad = \quad r\sqrt{1 - \frac{2\vec{r}.\vec{r}' + r'^2}{r^2}} \quad = \quad r - \vec{s}\cdot\vec{r}' + \epsilon$$

$$|\vec{r}-\vec{r}'| \quad \approx \quad r - \vec{s}\cdot\vec{r}',$$

where $\vec{s} = \vec{r}/r$

$$\frac{\exp(ik'|\vec{r}-\vec{r}'|)}{|\vec{r}-\vec{r}'|} \quad \approx \quad \frac{\exp(ikr)}{r} \exp(i\vec{k}\,' \cdot \vec{r}'). \tag{2.30}$$

Using the approximation (2.30) in (2.29), we see that

$$U_B(\vec{r}) \approx \exp(i\vec{k}_0 \cdot \vec{r}) + U_B^s(\vec{r}), \tag{2.31}$$

where

$$U_B^s(\vec{r}) = f_0(\vec{k}_0,\vec{k}\,';\omega)\frac{\exp(ikr)}{r} \tag{2.32}$$

and

$$f_0(\vec{k}_0,\vec{k}\,';\omega) = \iiint_{-\infty}^{\infty} F(\vec{r},\omega)U(\vec{r}\,')\exp(i\vec{k}\,' \cdot \vec{r}\,')d^3r\,' \tag{2.33}$$

is known as the scattering amplitude. For incident wave $U(\vec{r}\,') = \exp(i\vec{k}_0 \cdot \vec{r}\,')$ we have

$$f_0(\vec{k}_0,\vec{k}\,';\omega) = \iiint_{-\infty}^{\infty} F(\vec{r}\,',\omega)\exp[i(\vec{k}_0 - \vec{k}\,') \cdot \vec{r}\,']d^3r\,'. \tag{2.34}$$

Now function $f_0(\vec{k}_0,\vec{k}\,';\omega)$ has the form of 3D Fourier transform [27] of $F(\vec{r};\omega)$ with reciprocal, fourier variable $\vec{\mathcal{K}}$, i.e.

$$f_0(\vec{k}_0,\vec{k}\,';\omega) = \tilde{F}(\vec{\mathcal{K}},\omega) = \iiint_{-\infty}^{\infty} F(\vec{r}\,',\omega)\exp(i\vec{\mathcal{K}} \cdot \vec{r}\,')d^3r\,', \tag{2.35}$$

where

$$\vec{\mathcal{K}} = \vec{k}_0 - \vec{k}\,'. \tag{2.36}$$

It says that in the far-field, for a incident plane wave of direction $\vec{k}_0$, the amplitude of scattered field in a point of observation, determined by $\vec{k}\,'$, is proportional to the scattering amplitude [27]. This is true within the accuracy of the Born approximation.

2.5 Rytov Approximation

Formally, while one can expand the total field into a series of partial fields (Born case)

$$U = U_{(0)} + U_{(1)} + U_{(2)} + ..., \tag{2.37}$$

others can expand the total field into a series of exponentials instead [17]

$$U = \exp(\psi) = \exp(\psi_{(0)} + \psi_{(1)} + \psi_{(2)} + ...). \tag{2.38}$$

The expansion series (2.38) is the essence of the Rytov approximation. For the exact total field expressed by exponential using function $\psi = \psi(\vec{r})$ we have

$$U = \exp[\psi(\vec{r})], \tag{2.39}$$

where $\psi(\vec{r})$ have to carry information about space distribution of the amplitude and of the phase. This means, that $\psi(\vec{r})$ has to be a complex function. Now we have

$$U = \exp[\psi(\vec{r})] = \vec{A}(\vec{r})\exp[i\phi(\vec{r})], \tag{2.40}$$

where evidently

$$\psi(\vec{r}) \quad = \quad ln[\vec{A}(\vec{r})] + i\phi(\vec{r}). \tag{2.41}$$

Just like in case of the Born approximation, in general, the exact total field $U(\vec{r})$ inside a scatterer is unknown.

Now, let substitute field (2.39) into the (2.17). We obtain

$$\nabla^2\psi(\vec{r}) + \nabla\psi(\vec{r}) \cdot \nabla\psi(\vec{r}) + k^2n^2(\vec{r}) \quad = \quad 0, \tag{2.42}$$

where we used

$$\begin{aligned} \nabla^2 U(\vec{r}) \quad &= \quad \nabla \cdot \nabla U(\vec{r}) = \nabla \cdot \nabla \exp[\psi(\vec{r})] \\ &= \quad \nabla \exp[\psi(\vec{r})].\nabla\psi(\vec{r}) \\ &= \quad \exp[\psi(\vec{r})]\nabla\psi(\vec{r}).\nabla\psi(\vec{r}) + \exp[\psi(\vec{r})]\nabla^2\psi(\vec{r}). \end{aligned} \tag{2.43}$$

This is a nonlinear first order differential equation for $\nabla\psi$ and is known as the Ricatti equation.

As was mentioned in the previous section, the index of refraction differs slightly from unity, thus we can express the index of refraction as a space variation from unity as follows

$$n^2(\vec{r}) \quad = \quad [1 + \delta n(\vec{r})]^2 \quad \approx \quad 1 + 2\delta n(\vec{r}). \tag{2.44}$$

Now, Eq. (2.42) becomes

$$\nabla^2\psi(\vec{r},\omega) + \nabla\psi(\vec{r},\omega) \cdot \nabla\psi(\vec{r},\omega) + k^2[1 + 2\delta n(\vec{r},\omega)] \quad = \quad 0. \tag{2.45}$$

In the absence of the fluctuations ($\delta n = 0$) we have

$$\nabla^2\psi_0(\vec{r},\omega) + \nabla\psi_0(\vec{r},\omega) \cdot \nabla\psi_0(\vec{r},\omega) + k^2 \quad = \quad 0. \tag{2.46}$$

Let us re-write series for ψ, similar as in Born approximation, into two terms. First will stands for solution of homogeneous medium (as above) and second stands for solutions containing inhomogeneities, denoted with capital letter S. Explicitly

$$\psi \quad = \quad \psi_0 + \psi_S. \tag{2.47}$$

Equation (2.46) is independent of the medium and hence ψ_0 must be associated with incident field U^i, i.e.

$$\exp[\phi_0(\vec{r},\omega)] \quad = \quad U^i(\vec{r},\omega). \tag{2.48}$$

Next step is to insert (2.47) into (2.42) and take difference between result (2.46). We obtain

$$\nabla^2\psi_S(\vec{r},\omega) + \nabla\psi_0(\vec{r},\omega) \cdot \nabla\psi_S(\vec{r},\omega) \quad = \quad -\nabla\psi_S(\vec{r},\omega) \cdot \nabla\psi_S(\vec{r},\omega) + 2k^2\delta n. \tag{2.49}$$

Noting that

$$\nabla^2[U^i(\vec{r})\psi_S(\vec{r})] \quad = \quad \nabla^2U^i\psi_S(\vec{r}) + 2U^i i\nabla\psi_0(\vec{r}) \cdot \nabla\psi_S(\vec{r}) + U^i(\vec{r})\nabla^2\psi_S(\vec{r}). \tag{2.50}$$

It holds that $\nabla^2 U^i = k^2 U^i$. Last two terms of (2.50) are equal with (2.49), except for factor U^i. Equalling them we get

$$\nabla^2\psi_S(\vec{r}) + \nabla\psi_0(\vec{r})\cdot\nabla\psi_S(\vec{r}) \quad = \quad \frac{1}{U^i}[\nabla^2[U^i(\vec{r})\psi_S(\vec{r})] + k^2 U^i(\vec{r})\psi_S(\vec{r})]. \tag{2.51}$$

Substituing right-hand side of (2.51) into left-hand side of (2.49), we get

$$(\nabla^2 + k^2)[U^i(\vec{r})\psi_S(\vec{r})] \quad = \quad -[\nabla\psi_S(\vec{r})\cdot\nabla\psi_S(\vec{r}) + 2k^2\delta n]U^i. \tag{2.52}$$

We have already had these in Sec. 2.4, (2.23). It is inhomogeneous wave equation. Now, we can convert it automatically to the integral equation for ψ_S, i.e.

$$\begin{aligned}\psi_S(\vec{r}) \quad = \quad & \frac{1}{U^i}\iiint_{-\infty}^{\infty}[\nabla\psi_S(\vec{r})\cdot\nabla\psi_S(\vec{r}) + 2k^2\delta n]U_i \\ & \times \frac{\exp[ik(\vec{r}-\vec{r}\,')]}{|\vec{r}-\vec{r}\,'|}d^3r'.\end{aligned} \tag{2.53}$$

This is expression for the "scattered" part of ψ. Again, similar as in the Born approximation, we may assume that the first addend in the angle brackets is small compared to second one. Then, we can neglect this term. One then obtains first iteration called the Rytov approximation. Denoting it with capital R, we have

$$\psi_R(\vec{r}) \quad = \quad \frac{1}{U^i}\iiint_{-\infty}^{\infty} 2k^2\delta n U^i \frac{\exp[ik(\vec{r}-\vec{r}\,')]}{|\vec{r}-\vec{r}\,'|}d^3r'. \tag{2.54}$$

Inserting $\delta(\vec{r}) = \frac{1-n^2(\vec{r})}{2}$,

$$\psi_R(\vec{r}) \quad = \quad \frac{1}{U^i}\iiint_{-\infty}^{\infty} k^2[1-n(\vec{r})^2]U^i \frac{\exp[ik(\vec{r}-\vec{r}\,')]}{|\vec{r}-\vec{r}\,'|}d^3r'. \tag{2.55}$$

With $U^i = \exp(i\vec{k}_0.\vec{r})$ integral is known as first Born approximation for the scattered field U^s. We have

$$\psi_R(\vec{r}) \quad = \quad \frac{1}{4\pi}[U^i]^{-1}[U^s_B]. \tag{2.56}$$

The total field in the first Rytov approximation can be written as

$$U^R(\vec{r}) \quad = \quad \exp[\psi_0(\vec{r}) + \psi_R(\vec{r})] \quad = \quad U^i(\vec{r})\exp[\psi_R(\vec{r})]. \tag{2.57}$$

If we expand exponential in the series we can see that first two terms are indentical to first Born approximation for the total field, i.e.

$$U^i(\vec{r})\exp[\psi_R(\vec{r})] \quad = \quad U^i(\vec{r})(1+\psi_R(\vec{r}) + ...). \tag{2.58}$$

If we substitute (2.55) into (2.57) we have

$$U^i(\vec{r})(1+\psi_R(\vec{r}) + ...) \quad = \quad U^i(\vec{r}) + U_B(\vec{r}) + ... \tag{2.59}$$

This is the reason, why the first Rytov approximation is considered superior to the first Born approximation for incident wave being plane wave.

In practice, calculating ψ needs phase-unwrapping. It is because the imaginary part of ψ

$$\exp\{iIm[\psi(\vec{r})]\} \quad = \quad \exp(iIm\psi_i(\vec{r}) + iIm\psi_R(\vec{r})) \quad = \quad \exp\{i[\phi_i(\vec{r}) + \phi_R(\vec{r})]\} \tag{2.60}$$

is modulo 2π.

2.6 Validity of the Born and the Rytov approximation

Due to approximations we made in the previous two sections, it is natural that both methods underlie to restrictions in usage. Several papers deal with the validity of the Born and Rytov approximations [18, 28]. We briefly sum up some demands of both approximations, starting with the BA.

In the Born approximation, as the first iteration we replaced the total field inside the scatterer only by incident field $U = U^i + U^s \approx U^i$, this holds for

$$U^s(\vec{r}\prime) \quad \ll \quad U^i(\vec{r}\prime). \tag{2.61}$$

Any contribution to a field is a complex number. This implies, that above inequality must hold for both amplitude and phase. In case of amplitude, it means, that there is only little a absorption by the specimen. This is true for biological cells at near infrared, as was mentioned. In case of phase, it means, that there is only a little change in phase caused by change in optical path length due to inhomogeneities. For phase change approximated with ray optics, we have

$$\triangle\phi \quad \approx \quad \frac{2\pi}{\lambda}\left(\int n(\vec{r})ds - s_{total}n_m\right) \quad \ll \quad 2\pi. \tag{2.62}$$

For simplicity, let's think of specimen with fixed and homogeneous distribution of inhomogeneities. Thereby, (2.62) becomes

$$\triangle\phi \quad = \quad \frac{2\pi}{\lambda}s(n_s - n_m) \quad \ll \quad 2\pi. \tag{2.63}$$

This implies that

$$s(n_s - n_m) \quad \ll \quad \lambda. \tag{2.64}$$

It means that optical path difference is much smaller than the wavelength λ. Therefore the validity of the Born approximation underlies the restriction of optically thin samples.

In case of the Rytov approximation it is a little bit more complicated considering its non-linear, but exponential description of wave propagation. Nevertheless, certain analyses have shown that the Rytov approximation should be valid for optically thicker samples than in case of the Born approximation. Moreover, it requires that $|\nabla\psi_S| \ll 2\pi/\lambda$ [19]. This holds for large scale at which δn fluctuates compared to the wavelength λ . It is evident that for the shorter wavelength λ usage of the Rytov approximation should becomes more valid.

2.7 FDTD

2.7.1 Introduction to the FDTD method

Electromagnetic simulations solving Maxwell equations have become an essential tool with applications ranging from telecommunications to radar systems [29], design of high speed electronic circuit boards [30], scattering simulations of biological samples [31] and much more.

In early days, large-scale of Maxwell's equations solutions have been motivated by the requirements of military defense. Especially, the need of understanding the scattering of electromagnetic waves by complex, electrically large material structures for a defensive radar system development using mechanical calculators.

With the rise of computers, primarily, it was frequency domain used for solving Maxwell's equations. Later, it turned out that approaches based on the frequency domain have difficulty treating nonmetallic material composition and volumetric complexity of a structure. This led to early explorations of a novel alternative approach, direct time-domain solutions of Maxwell's differential equations, called finite difference time domain (FDTD) [29].

FDTD method was first presented by Yee in 1966 [32]. He proposed the discretization algorithm for Maxwell's equations, today called Yee's algorithm. It solves the Maxwell's equations in a direct manner by discretizing the physical space with regular elementary volumes.

Since then, many alternative griddings of the Maxwell's equations have been proposed. However, none have had the seminal impact and longevity of his "original family recipe".

The growth of the FDTD method since the late 1970's can certainly be paralleled to the ongoing advances in computer technology. There are several primary reasons for the expansion of interest in FDTD method, such as being fully explicit, can cover a wide frequency range with a single simulation run, and treat nonlinear material properties in a natural way, since it is a time-domain method.

2.7.2 Yee's algorithm

Yee's algorithm is based on discretizing the volume domain with a regular, structured, rectangular grid, using central difference operators having second-order accuracy. To maintain the accuracy, the electric and magnetic fields must be staggered in both space and time.

Yee's algorithm is derived from electromagnetic induction, which relates electric and magnetic fields. Using differential form of Maxwell's curl equations (2.1) and (2.2) we have six equation for each component of electric and magnetic field in Cartesian coordinates.

$$\frac{\partial \mathcal{E}_x}{\partial t} = \frac{1}{\epsilon}\left(\frac{\partial \mathcal{H}_z}{\partial y} - \frac{\partial \mathcal{H}_y}{\partial z}\right) \tag{2.65}$$

$$\frac{\partial \mathcal{E}_y}{\partial t} = \frac{1}{\epsilon}\left(\frac{\partial \mathcal{H}_x}{\partial z} - \frac{\partial \mathcal{H}_z}{\partial x}\right) \tag{2.66}$$

$$\frac{\partial \mathcal{E}_z}{\partial t} = \frac{1}{\epsilon}\left(\frac{\partial \mathcal{H}_y}{\partial x} - \frac{\partial \mathcal{H}_x}{\partial y}\right) \tag{2.67}$$

$$\frac{\partial \mathcal{H}_x}{\partial t} = \frac{1}{\mu}\left(\frac{\partial \mathcal{E}_z}{\partial y} - \frac{\partial \mathcal{E}_y}{\partial z}\right) \tag{2.68}$$

$$\frac{\partial \mathcal{H}_y}{\partial t} = \frac{1}{\mu}\left(\frac{\partial \mathcal{E}_x}{\partial z} - \frac{\partial \mathcal{E}_z}{\partial x}\right) \tag{2.69}$$

$$\frac{\partial \mathcal{H}_z}{\partial t} = \frac{1}{\mu}\left(\frac{\partial \mathcal{E}_y}{\partial x} - \frac{\partial \mathcal{E}_x}{\partial y}\right). \tag{2.70}$$

In order to best approximate curl of electric (magnetic) field at a point where magnetic (electric) field is being computed, the central difference formula is used (Fig. 2.2). For an arbitrary differentiable function f we have

$$\frac{\partial f_x}{\partial x} \approx \frac{f(x + \triangle/2) - f(x - \triangle/2)}{\triangle}, \tag{2.71}$$

where $\triangle$ is optional difference step defining size of the grid (Fig. 2.3). For a uniform, rectangular grid, each point of the grid can be denoted as follows

$$(i,j,k) = (i\triangle x, j\triangle y, k\triangle z), \tag{2.72}$$

where i, j and k are integers. Similarly, time is uniformly discretized as $t = n\triangle t$. then the function $f(x,y,z,t)$ can be expressed at any point within the grid using the notation:

$$f(x,y,z,t) = f(i\triangle x, j\triangle y, k\triangle z, n\triangle t) = f^n_{i,j,k}. \tag{2.73}$$

Descretizing equations (2.65)-(2.70) using (2.71) and notation of (2.73) we have [34]

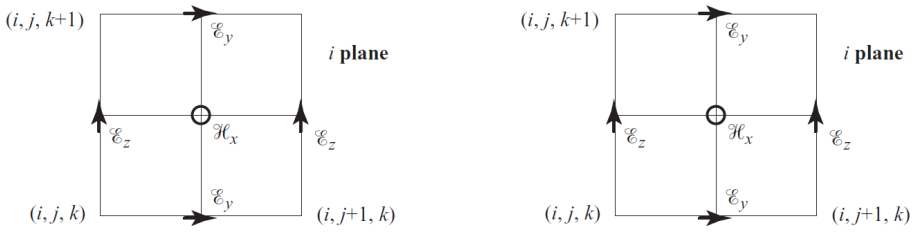

Figure 2.2: 2D Yee grid. Curl of electric field(left), curl of magnetic field(right) [33].

$$\mathcal{E}^{n+1/2}_{x,i+1/2,j,k} = \mathcal{E}^{n-1/2}_{x,i+1/2,j,k} + \frac{\triangle t}{\epsilon}\left(\frac{\mathcal{H}^n_{z,i+1/2,j+1/2,k} - \mathcal{H}^n_{z,i+1/2,j-1/2,k}}{\triangle y} - \right. \\ \left. - \frac{\mathcal{H}^n_{y,i+1/2,j,k+1/2} - \mathcal{H}^n_{y,i+1/2,j,k-1/2}}{\triangle z}\right) \tag{2.74}$$

$$\mathcal{E}^{n+1/2}_{x,i,j+1/2,k} = \mathcal{E}^{n-1/2}_{x,i,j+1/2,k} + \frac{\triangle t}{\epsilon}\left(\frac{\mathcal{H}^n_{x,i,j+1/2,k+1/2} - \mathcal{H}^n_{x,i,j+1/2,k-1/2}}{\triangle z} - \right. \\ \left. - \frac{\mathcal{H}^n_{z,i+1/2,j+1/2,k} - \mathcal{H}^n_{z,i-1/2,j+1/2,k}}{\triangle x}\right) \tag{2.75}$$

$$\mathcal{E}^{n+1/2}_{x,i,j,k+1/2} = \mathcal{E}^{n-1/2}_{x,i,j,k+1/2} + \frac{\triangle t}{\epsilon}\left(\frac{\mathcal{H}^n_{y,i+1/2,j,k+1/2} - \mathcal{H}^n_{y,i-1/2,j,k+1/2}}{\triangle x} - \right. \\ \left. - \frac{\mathcal{H}^n_{x,i,j+1/2,k+1/2} - \mathcal{H}^n_{x,i,j-1/2,k+1/2}}{\triangle y}\right) \tag{2.76}$$

$$\mathcal{H}^{n+1}_{x,i+1/2,j,k} = \mathcal{H}^n_{x,i+1/2,j,k} + \frac{\triangle t}{\epsilon}\left(\frac{\mathcal{H}^n_{z,i+1/2,j+1/2,k} - \mathcal{H}^n_{z,i+1/2,j-1/2,k}}{\triangle y} - \right. \\ \left. - \frac{\mathcal{H}^n_{y,i+1/2,j,k+1/2} - \mathcal{H}^n_{y,i+1/2,j,k-1/2}}{\triangle z}\right) \tag{2.77}$$

$$\mathcal{H}^{n+1}_{x,i,j+1/2,k} = \mathcal{H}^n_{x,i,j+1/2,k} + \frac{\triangle t}{\epsilon}\left(\frac{\mathcal{H}^n_{x,i,j+1/2,k+1/2} - \mathcal{H}^n_{x,i,j+1/2,k-1/2}}{\triangle z} - \right. \\ \left. - \frac{\mathcal{H}^n_{z,i+1/2,j+1/2,k} - \mathcal{H}^n_{z,i-1/2,j+1/2,k}}{\triangle x}\right) \tag{2.78}$$

$$\mathcal{H}^{n+1}_{x,i,j,k+1/2} = \mathcal{H}^n_{x,i,j,k+1/2} + \frac{\triangle t}{\epsilon}\left(\frac{\mathcal{H}^n_{y,i+1/2,j,k+1/2} - \mathcal{H}^n_{y,i-1/2,j,k+1/2}}{\triangle x} - \right. \\ \left. - \frac{\mathcal{H}^n_{x,i,j+1/2,k+1/2} - \mathcal{H}^n_{x,i,j-1/2,k+1/2}}{\triangle y}\right). \tag{2.79}$$

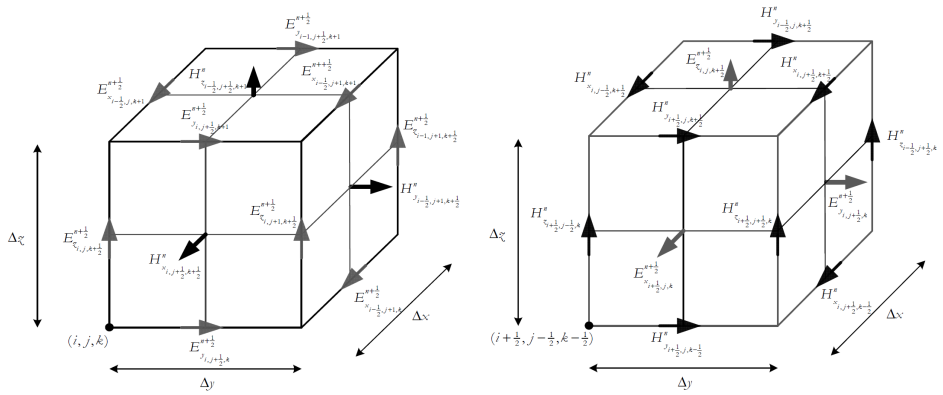

Figure 2.3: Primary(left) and secondary(right) grid cell of the regular, structured, rectangular, staggered grip [34].

Stability and grid size

To obtain correct, converging simulation results, one has to ensure numerical stability of a simulation. Crucial is the size of time and space discretization step. Sizes must be small such that electromagnetic field does not change significantly over one grid cell. This means that the wavelength of a source must be much higher than spatial discretization of a grid, otherwise velocity propagation of numerical waves could be affected in an unwanted manner [29]. There is also a relation between time step $\triangle t$ and spatial step $\triangle x$, which must be hold to achieve numerical stability. It is [34]

$$\triangle t \quad = \quad \frac{1}{c}\frac{1}{\sqrt{\frac{1}{\triangle x^2}+\frac{1}{\triangle y^2}+\frac{1}{\triangle z^2}}}, \tag{2.80}$$

where c is the speed of light. This defines the Courant-Fredrichs-Lewy (CFL) stability limit of the three-dimensional Yee algorithm for Maxwell's equations. This limit restricts the choice of the time-step. For a cubic grid, i.e. $\triangle x = \triangle y = \triangle z = \triangle$, the stability limit becomes

$$\triangle t \quad = \quad \frac{\triangle}{c}\frac{1}{\sqrt{3}}. \tag{2.81}$$

2.7.3 Total-field Scattered-field TF/SF

For simulations requiring plane-wave source, there was designed the so-called total-field/scattered-field technique (TF/SF), (earlier Huygen surface). This technique resulted from attempts to introduce a plane-wave source that avoids the difficulties caused by initial condition approach discussed in [29].

TF/SF technique is based on the linearity of Maxwell's equations. Thus, electric and magnetic fields can be expressed as a superposition of incident and scattered fields

$$\vec{\mathcal{E}}_{total} \quad = \quad \vec{\mathcal{E}}_{inc} + \vec{\mathcal{E}}_{scatt}, \qquad \vec{\mathcal{H}}_{total} \quad = \quad \vec{\mathcal{H}}_{inc} + \vec{\mathcal{H}}_{scatt}, \tag{2.82}$$

where $\vec{\mathcal{E}}_{inc}, \vec{\mathcal{H}}_{inc}$ forms the plane wave propagating in the homogeneous free space with the absence of any inhomogeneities. These are assumed to be known at all points of the grid at all time-steps. The scattered fields $\vec{\mathcal{E}}_{scatt}, \vec{\mathcal{H}}_{scatt}$ are the perturbations of the field due to interaction of the incident field with any inhomogeneity. These are initially unknown.

2D TF/SF formulation is schematically shown in the Fig. (2.4). Whole simulation region is divided into two distinct subregions, Region 1 and Region 2 bounded by desired boundary conditions discussed below.

Region 2 is a certain part of grid where total fields are assumed to be stored in the computer memory at specific plane called monitor. Here Yee algorithm operates on total-field vector components. Any inhomogeneities must be embedded within this region. The incident plane wave is launched at the bottom edge of this region. If the grid is not aligned, so that incident wave is along one of the principal axes, the incident fields can be analytically computed at each cell position [33]. This makes possible to simulate problems with non-normal incidence.

Region 1 is a remaining part of a grid, where only scattered fields are assumed to be stored in the computer memory. Here, Yee algorithm operates only on scattered-field vector components.

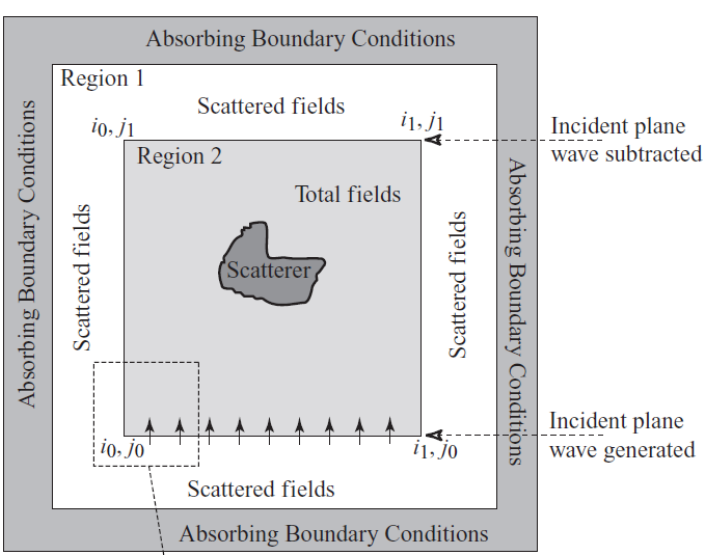

(a) Illustrating TF/SF technique [33].

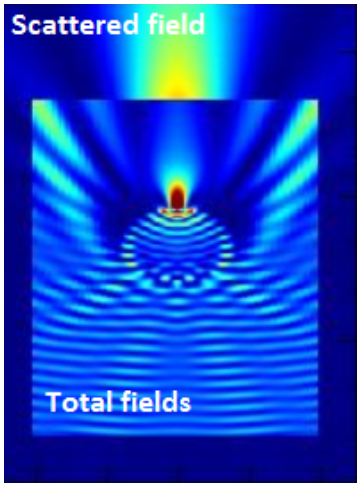

(b) Illustrating the elimination of a scattered field at the boundaries [35].

Figure 2.4: Primary(left) and secondary grid cell of the regular, strctured, rectangular, staggered grip

There are several advantages using TF/SF source summarized in [29], for instance near-field to far-field transformation monitor can be located within Region 1 and therefore having values of fields outside the simulation. Setting arbitrary time waveform and duration, angle of incidence or angle of polarization, etc. Because of finiteness of a simulation there must be specific boundary conditions, depending on requirements, at the outermost grid planes. For instance, it might be a metal boundary conditions that behave as a Perfect Electric Conductor (PEC), i.e. as a perfectly reflecting surface. Analogously Perfect Magnetic Conductor (PMC). Many problems are interested in simulation of free space which means boundary conditions are placed at infinity to avoid the reflection toward the inned domain. To simulate a free space one can use special case of absorbing boundary conditions (ABC), called Perfectly Matched Layer (PML) [36].

PML

These boundaries absorb electromagnetic waves incident upon them, thus there are no reflections on boudaries. They are described as a lossy medium dependent on the angle of incidence and angular frequency of incident wave. On the other hand, the attenuation of such a wave is dependent on thickness of PML boundaries and its conductivity and its artificially added magnetic nonphysical conductivity. The higher thickness and conductivity, the higher attenuation. But there must be rather smooth variation of conductivity at the medium-PML interface, otherwise, spurious numerical reflections can occur. High thickness of PML rather results in computational cost.

3. Simulation and results

3.1 Simulation using Born approximation and Rytov approximation

For simulation of scattering in BA and RA, we used home-made software Matlab. Both simulations were computed for various directions of the incident plane waves with unity amplitude of $U^i_{B,R}$. Every direction of the plane wave can be described by the wave vector $\vec{k} = (k_x,k_y,\sqrt{k^2 - k_x^2 - k_x^2})$, thus any direction is uniquely described by the vector $\vec{k_t} = (k_x,k_y)$, where t stands for transverse. In the next sections only $\vec{k_t}$ will be used.

Parameters of simulation

Scattering of the idealized model of cell was simulated (Fig. 3.1). The cell is placed in the plane $z = 0$, consists of the two different structures, shapes and indexes of refractions. The greatest one is called mitochondrion having elliptical shape with semi-major axis a and semi-minor axes b, c and having index of refraction $n = 1.37$. The second one is called organelle having spherical shape and index of refraction $n = 1.42$. The index of refraction of background is $n = 1.336$. The cell contains three identical organelles parallel along axis x with equidistant spacing. Other parameters of the simulation are in the Tab. (3.1).

wave length λ [nm]	1000
cubic grid cell size $\triangle$ [nm]	125
mitochondrion (a,b,c) [μm]	(5, 3.5, 3.5)
organelle radius [μm]	0.75
position of mid organelle (x,y,z) [μm]	(0, 0, -1.2)
organelle spacing (x,y,z) [μm]	($\pm$3, 0, -1.2)

Table 3.1: Simulation parameters.

Monitor was placed at the distance $z = 150$ nm and its dimensions are $L_x = 32$ μm $L_y = 16$ μm. There is $N_x = 128$ points in x directions and $N_y = 64$ points in y directions. Together it is 8192 points on the monitor where fields $U^{i,j}_{B,R}$ were computed, where i,j denotes the position of a point on the monitor. Points are equidistantly spaced, i.e. $\triangle x = \triangle y = 250$ nm.

Directions of individual plane waves were computed using relation between direct

and reciprocal k-space, i.e.

$$\triangle k_x = \frac{2\pi}{\triangle x N_x}, \qquad \triangle k_y = \frac{2\pi}{\triangle y N_y} = 2\triangle k_x \tag{3.1}$$

$$\vec{k}_t^{q,p} = (q\triangle k_x, p\triangle k_y), \qquad q = 0,1,...,26, \qquad p = 0,1,...,13. \tag{3.2}$$

For $q = p = 0$ we have plane wave propagating in the z direction, we will consider such wave as wave of normal incidence. This relations fulfill Nyquist-Shannon sampling theorem [37]. Higher sampling does not provide any change in results.

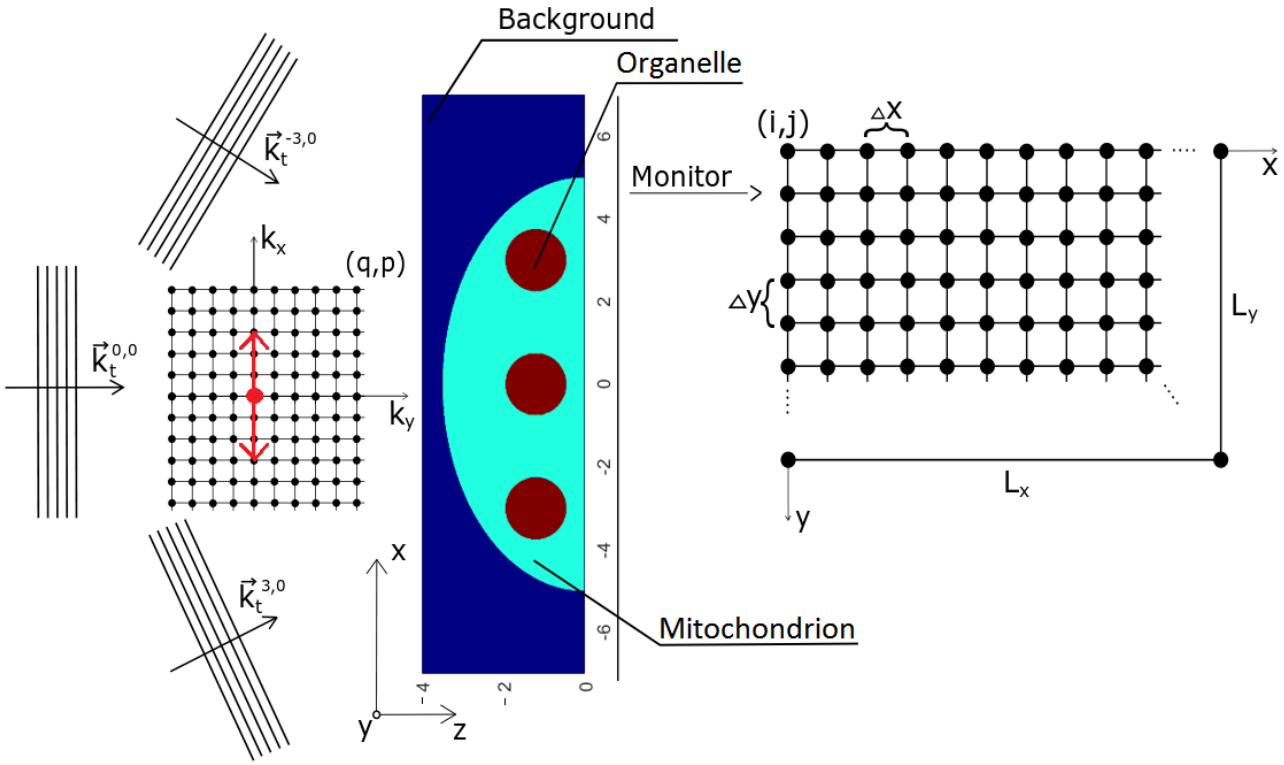

Figure 3.1: 2D projection of the cell with monitor shown and three different direction of incident plane waves.

3.2 FDTD simulation

Rigorous FDTD method calculations were performed in the 3D Lumerical FDTD Solution software [35]. Similar as in the previous section, we will use $\vec{k}_t$ notation.

Parameters of FDTD simulation

For simulation we used the same parameters as described in previous section, except for the size of grid cell and number of point on the monitor. Equally, shape of the grid was cubic with size of the spatial step $\triangle = 50$ nm. Here $N_x = 640$ $N_y = 320$. All points in BA and RA monitor intersect with the points of FDTD monitor and only these were chosen for further processing. Number of PML layers were set up to 16. Polarization was chosen in the direction of the y axis. Auto-shutoff criteria were: simulation duration $t = 2000$ fs and energy left in the simulation domain $E = 1.10^{-5}$ of initial value. Dimension of simulation domain was $X = 34$ μm, $Y = 7$ μm, $Z = 18$ μm.

3.3 Results

The main goal in this section is to compare accuracy of BA and RA to FDTD method. All 2D images are just a fraction of the whole monitor due to lucidity, whereas all 1D cross-section images are of range of the width/height of the monitor. All figures are ordered in the following manner: BA, RA, FDTD method.
In the Fig. (3.2), there are images of absolute value of the total fields U_B^t, U_R^t, U_L^t for three angles of incidence 0°, 15° and 37°. Its particular maximal and minimal values shown in the Tab. (3.2). It can be seen, that the range of the field values across the whole monitor of the Rytov method corresponds to the FDTD method more than the Born method. The cross-section of the fields for normal incidence is shown in the

	maximum	minimum
(U_B^t,U_R^t,U_L^t) $\alpha = 0°$	(1.82, 1.55, 1.39)	(0.88, 0.89, 0.90)
(U_B^t,U_R^t,U_L^t) $\alpha = 15°$	(1.76, 1.50, 1.37)	(0.86, 0.87, 0.89)
(U_B^t,U_R^t,U_L^t) $\alpha = 37°$	(1.84, 1.55, 1.40)	(0.81, 0.81, 0.82)

Table 3.2: Maximal and minimal values of particular total fields.

	maximum	minimum
(U_B^t,U_R^t,U_L^t) $\alpha = 0°$	(1.16, 1.39, 1.25)	(0.00, 0.00, 0.00)
(U_B^t,U_R^t,U_L^t) $\alpha = 15°$	(1.15, 1.32, 1.24)	(0.00, 0.00, 0.00)
(U_B^t,U_R^t,U_L^t) $\alpha = 37°$	(1.22, 1.41, 1.32)	(0.00, 0.00, 0.00)

Table 3.3: Maximal and minimal values of particular scattered fields.

Fig. (3.3). Here, it can be seen that even the field distribution is more accurate in

the case of RA. BA does not contain some detail information in the regions between maximal values of the field. Here, we have to say that whether it is scattered or total field, values are almost equal at the edges of monitor for all cases of incidence.

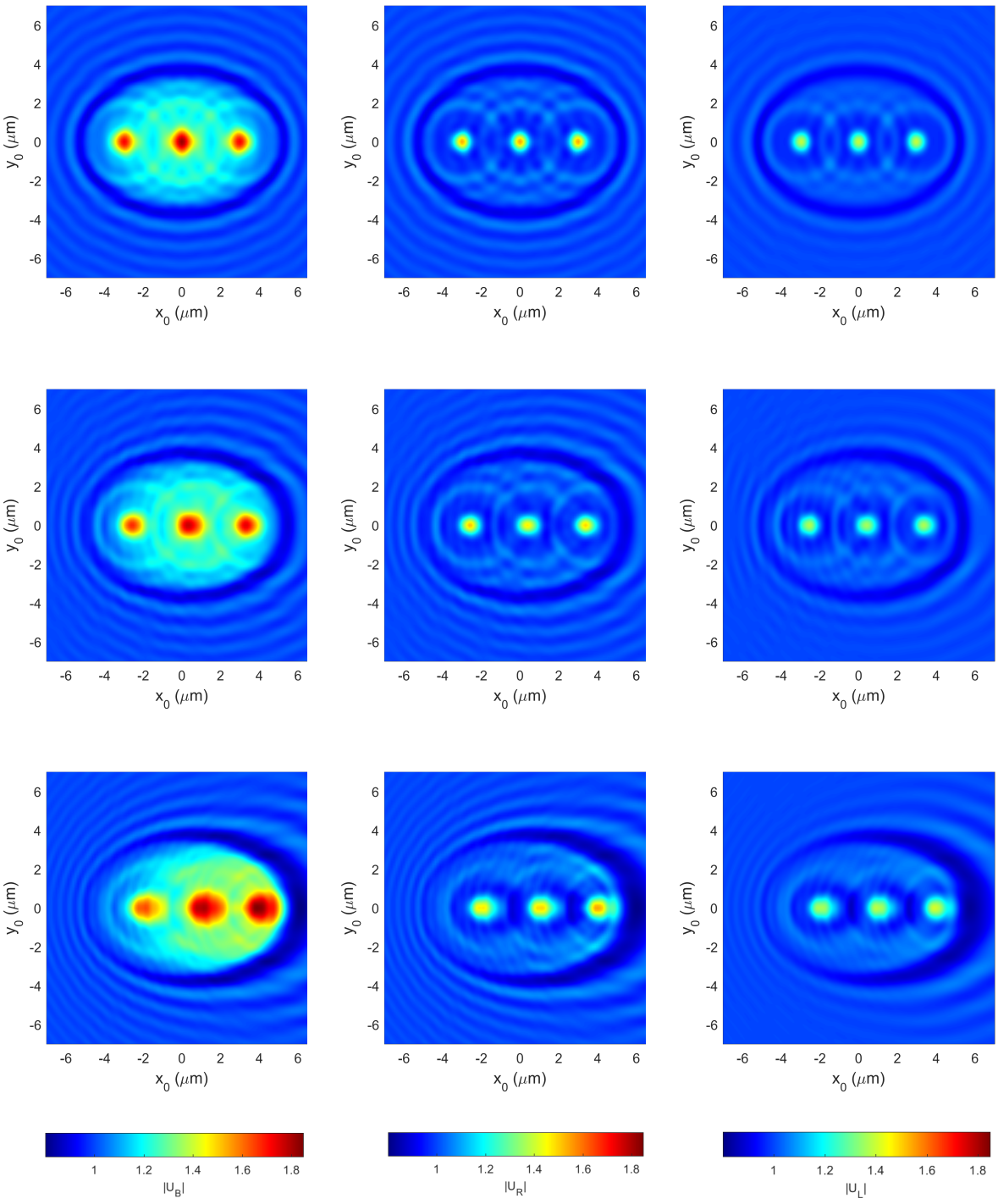

Figure 3.2: The absolute value of total field at distance $z = 150$ nm behind the cell. Columns represents results of BA(left), RA(middle), FDTD method(right) for the angle of incidence: 0°, 15° and 37°; $q = 0$, 12, 26.

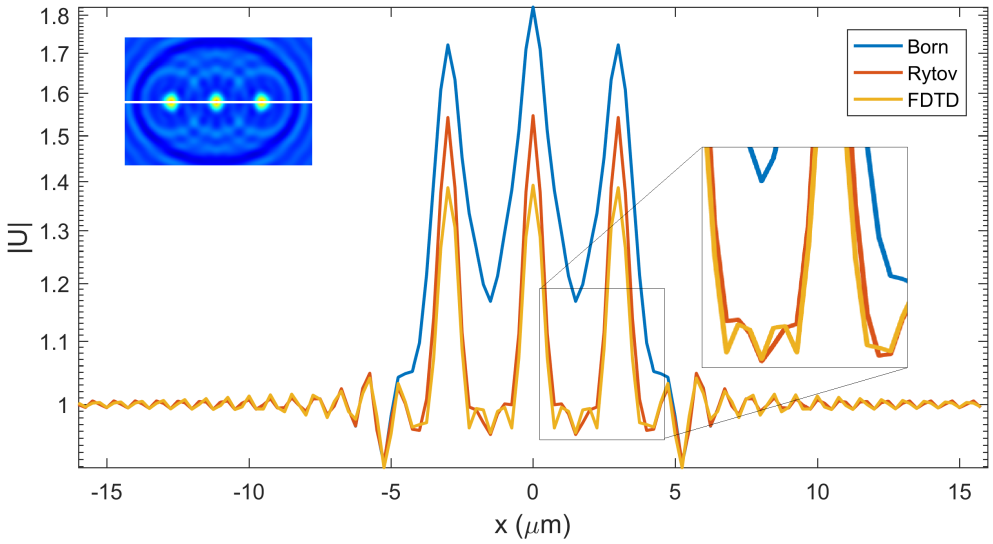

Figure 3.3: Slice through absolute value of the total fields of the BA, RA, FDTD method; normal incidence ($q = 0$, $p = 0$). Sub-figure: schematically shown slice.

Despite of all above conclusions, from the Fig. (3.4) and (3.5), and Tab. 3.3, it can be seen, that it is the RA which has wider range of absolute values of the scattered field. Concerning the field distribution it is similar for both. As was discussed in the previous chapters, the total field is just a sum of the scattered field and the incident plane wave. RA reach higher maximal value of the scattered field than BA, whereas BA reach higher maximal value of the total field, this means, that there must be different phase distribution of the scattered fields (Fig. 3.6) of approximative methods, because phase of the incident wave is equal for both. As we saw, the resultant superposition of these two field is more accurate in the RA for the normal incidence.

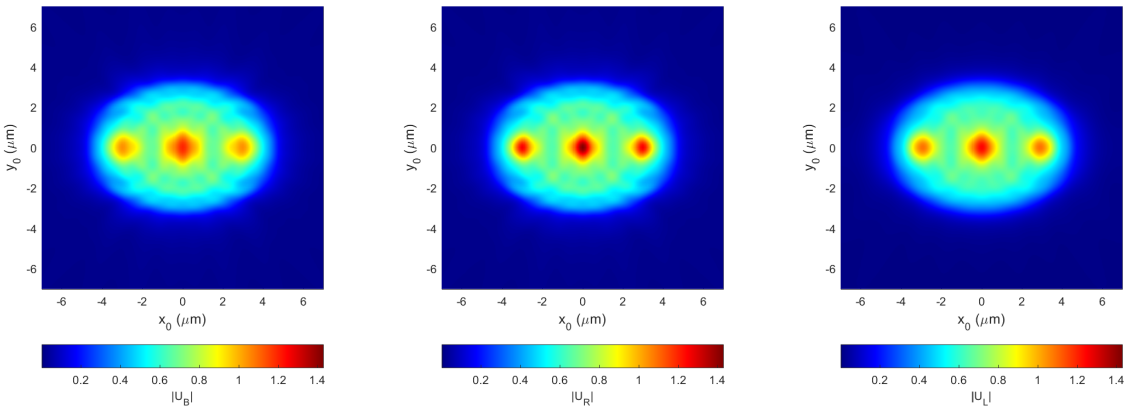

Figure 3.4: Absolute value of scattered field at distance z=150nm behind the cell: BA(left), RA(middle), FDTD method(right); normal incidence ($q = 0$, $p = 0$).

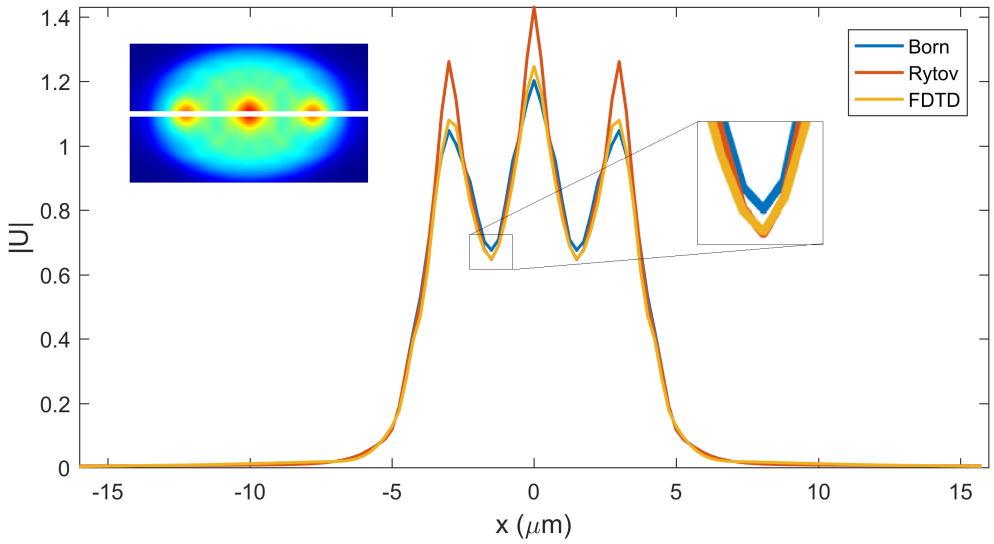

Figure 3.5: Slice through the absolute value of the scattered field of the BA, RA, FDTD method; normal incidence ($q = 0$, $p = 0$).

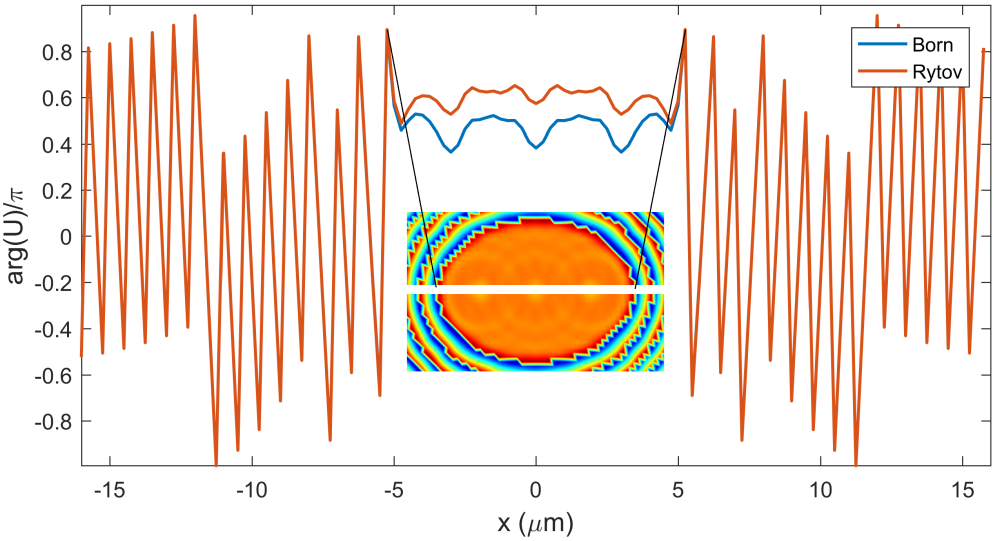

Figure 3.6: Slice through the phase of the scattered fields of the BA and RA; normal incidence ($q = 0$, $p = 0$).

Now, we shall show the contributions to the field from particular parts of the cell: mitochondrion and three organelles. The first one was obtained by setting organelle's index of refraction to that of mitochondrion. The second one was obtained by setting mitochondrion's index of refraction to that of the background. We have to say that, for several reasons, the sum of the fields from the particular contributions are not equal to that obtained by the cell as a whole. But, it may be helpful to realize which parts of the cell cause greater deviations from FDTD method for the RA and BA.
First, we start with the mitochondrion. In the Fig. (3.7), we can see the absolute values of the total and scattered fields $U_B^{t,s}$, $U_R^{t,s}$, $U_L^{t,s}$. Here, it can be seen again, that BA

rises error mainly in its phase. In this case, the Rytov method is more accurate in the scattered field than the Born method (Fig. 3.8b), which does not hold for the whole cell with organelles.

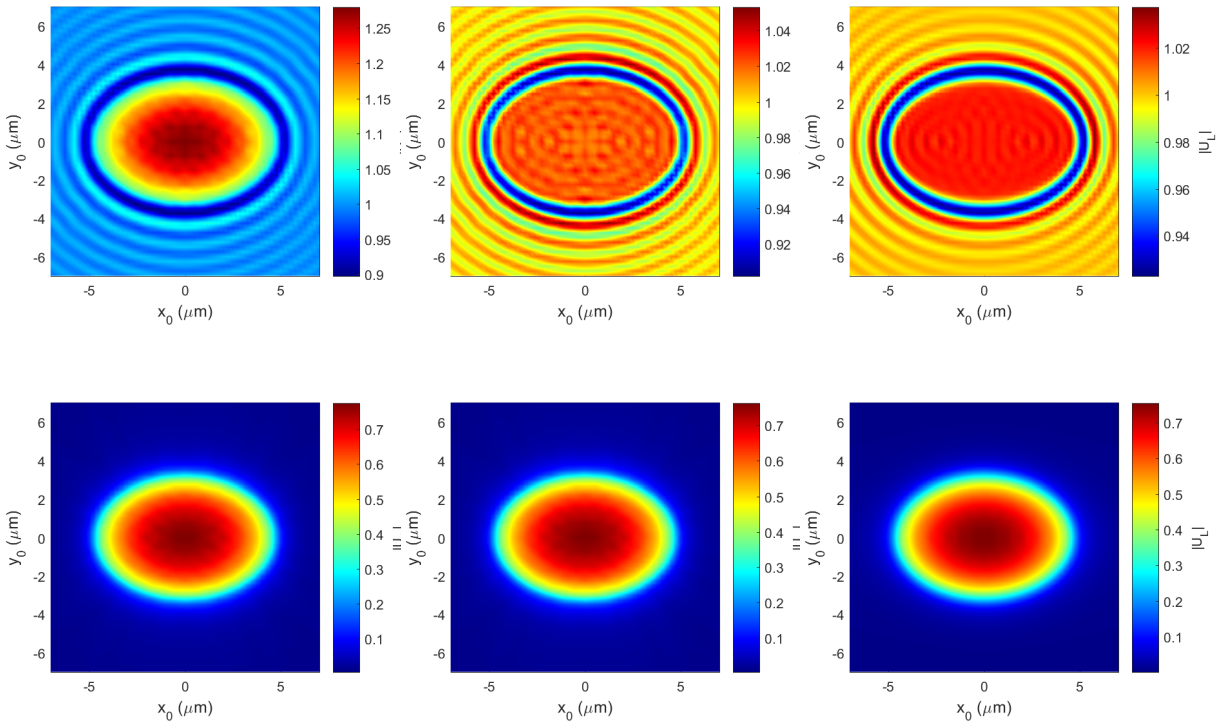

Figure 3.7: Mitochondrion: absolute value of the total(top) and scattered(bottom) field at distance $z = 150$ nm behind the mitochondrion: BA(left), RA(middle), FDTD method(right); normal incidence ($q = 0$, $p = 0$).

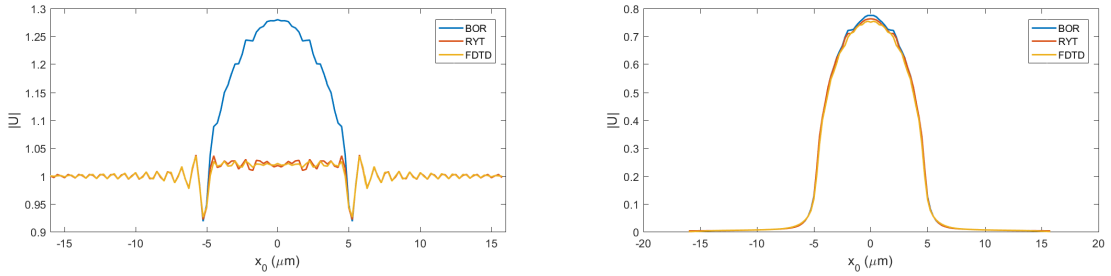

(a) Total field

(b) Scattered field

Figure 3.8: Mitochondrion: slices through the absolute values of the total and scattered fields; normal incidence ($q = 0$, $p = 0$).

In case of the organelles, we show only the slice figures. As expected it is obvious from the Fig. (3.9a), that RA scatters more than the BA and FDTD method. Also, we can see again that BA "forgot" about that one local minimum compared to Fig. (3.9b), where it did not. In the last Fig. (3.10), there are the slices through the phase of the field of particular methods. Here, the FDTD method field had to be multiplied by the

phase factor $\exp^{-i\phi}$ to align phases, where ϕ is the phase of the incident plane wave at $z = 150$ nm. It can be seen, that BA phase stops to trace FDTD line at $x = -3.5$ μm, approximately. It is because an organelle starts to be optically too thick for the BA.

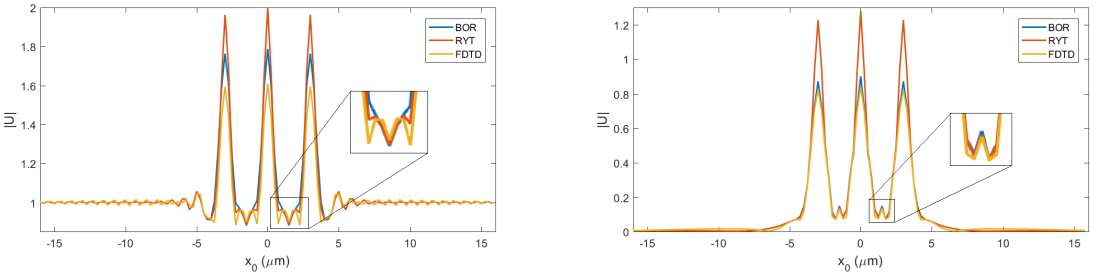

(a) Total field (b) Scattered field

Figure 3.9: Organelles: slices through the absolute values of the total and scattered fields; normal incidence ($q = 0$, $p = 0$).

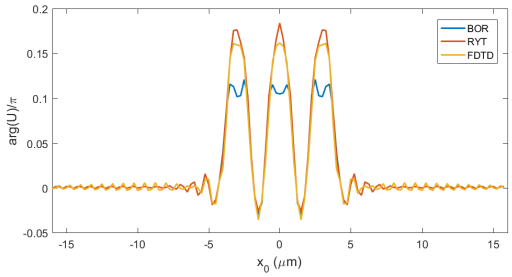

Figure 3.10: Organelles: slice through the phase of the scattered fields of BA, RA, FDTD method; normal incidence ($q = 0$, $p = 0$).

Thus, we can conclude that for the optically thick objects the resulting complex field U_B is rather inaccurate. For the optically thick and optically less dense objects, relative to surrounding, the RA is clearly more appropriate for a use. On the other hand for the optically higher dense object, the RA rather scatters too much. This corresponds to that discussed in the Sec. 2.6.

In the following we will discuss the case of oblique incidence of plane wave ($q \neq 0$, $p \neq 0$). At the end, there will be analyzed the influence of changing the wavelength λ of the incident plane wave. All the other slice figures of the resulting fields are displayed from the line passing through overall maximal value in the x axis direction. Due to the vectorial character of the FDTD method only E_y component of the field is chosen to obtain scalar expression of the field. The difficulty emerges when the direction of propagation of the incident wave is no longer only in the (x,z) direction; $p \neq 0$. This means that the polarization direction of incident wave is generally expressed by $\vec{E} = (E_x \neq 0, E_y \neq 0, E_z \neq 0)$. From the FDTD method, we can obtain all three projections of $\vec{E}$ in the observation plane. Now, E_y is not of magnitude of the unity and it would bring errors in the comparison of the resulting fields. For this purposes, all the slice figures are obtained by normalizing the particular fields.

In the Fig (3.11), we can see the comparison for plane wave of the maximal angle of incidence; $q = 26, p = 13$. Here the colors of the image depends only on the relative differences between particular values. The range of colors is linearly distributed between maximal and minimal value. It can be seen, that Born method is rather inaccurate.

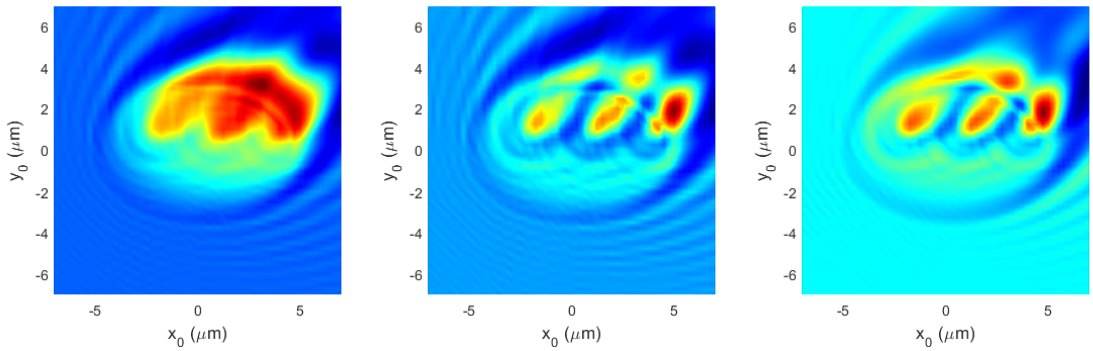

(a) BA (b) RA (c) FDTD

Figure 3.11: Absolute value of the total field at distance $z = 150$ nm behind the cell; $q = 26$, $p = 13$.

The slice graphs (Fig. 3.12) describe the inaccuracy better. The graph shows absolute value of the field that was normalized to hold

$$\sum_{i=1}^{128}\sum_{j=1}^{64}|U_{B,R,L}|^2 \quad = \quad 1. \tag{3.3}$$

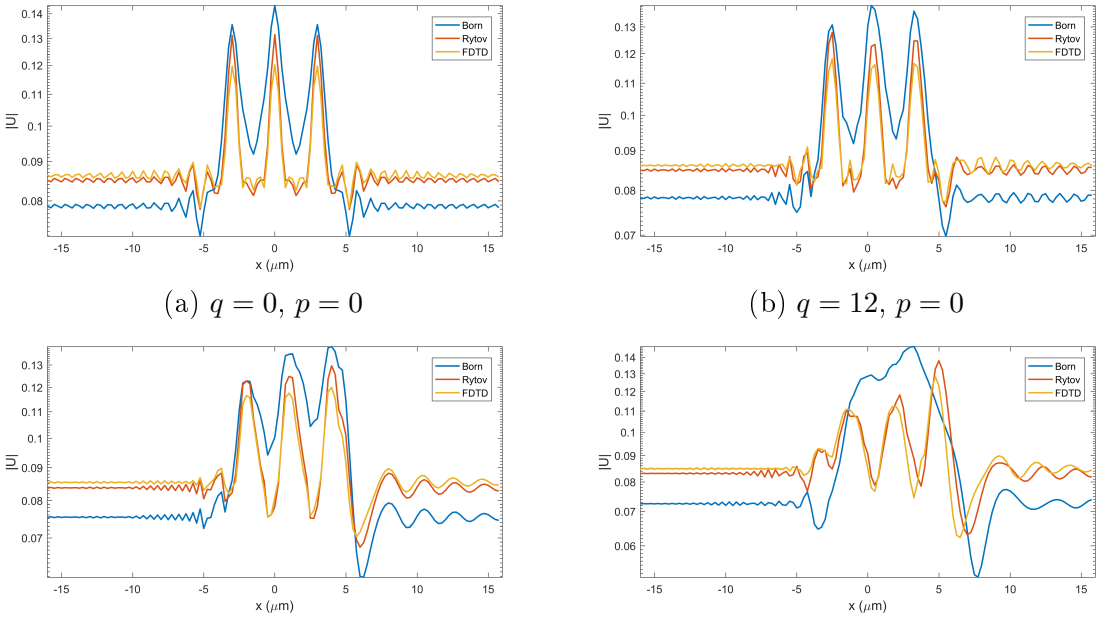

(a) $q = 0$, $p = 0$ (b) $q = 12$, $p = 0$

(c) $q = 26$, $p = 0$ (d) $q = 26$, $p = 13$

Figure 3.12: Slices through the absolute values of the total fields for 4 directions of the angle of incidence (q, p).

From the Fig. (3.12c) and (3.12d) it seems, like RA is slightly shifted compared to FDTD method, but a slice do not have to be displayed from the same line. To quantify differences between the methods, we define the error by

$$E = \sum_{i=1}^{128}\sum_{j=1}^{64}\frac{|U^{B,R} - U^{L}|}{N_p}, \tag{3.4}$$

where N_p is the number of points on the monitor. Complex total fields $U_{B,R,L}$ had to be phase aligned. Resulting error is shown in the Fig. (3.13) for three tilts in y axis direction corresponds to values $p = 0, 7, 13$.

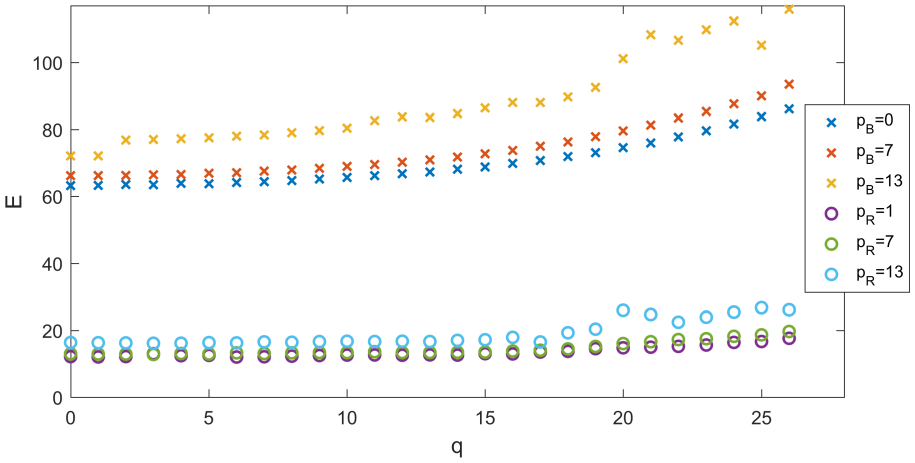

Figure 3.13: Values of the error E for all q and $p = 0, 7, 13$. Error of the BA is cross-marked and the RA circle-marked.

We can see very slight upward tendency in the RA for the particular p. It is more obvious in the BA case. There is an overall increasing error for increasing angles in both methods. Magnitude of Born error is approximately three times higher than Rytov error.

Now we will analyze the influence of the wavelength λ on the resulting field. From the error Fig. (3.14), we can see the downward tendency for both methods. Particular field are shown in the Fig. (3.15). It is not surprising in the BA, because it holds that with the increasing wavelength λ, an object becomes optically thinner. Whereas, in the Sec. 2.6, we introduced the condition $|\nabla\psi_S| \ll 2\pi/\lambda$ for the Rytov approximation. The results are in contradiction with the condition. It is not the only condition ensuring higher coincidence of results. Even though it may hold for some special cases.

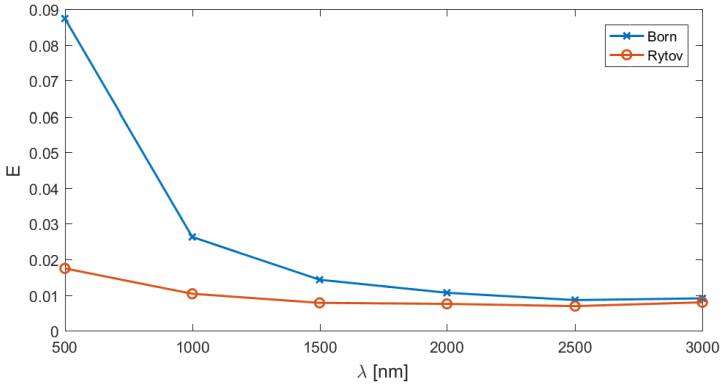

Figure 3.14: Values of the error E for $q = 0, p = 0$ as a function of wavelengths λ.

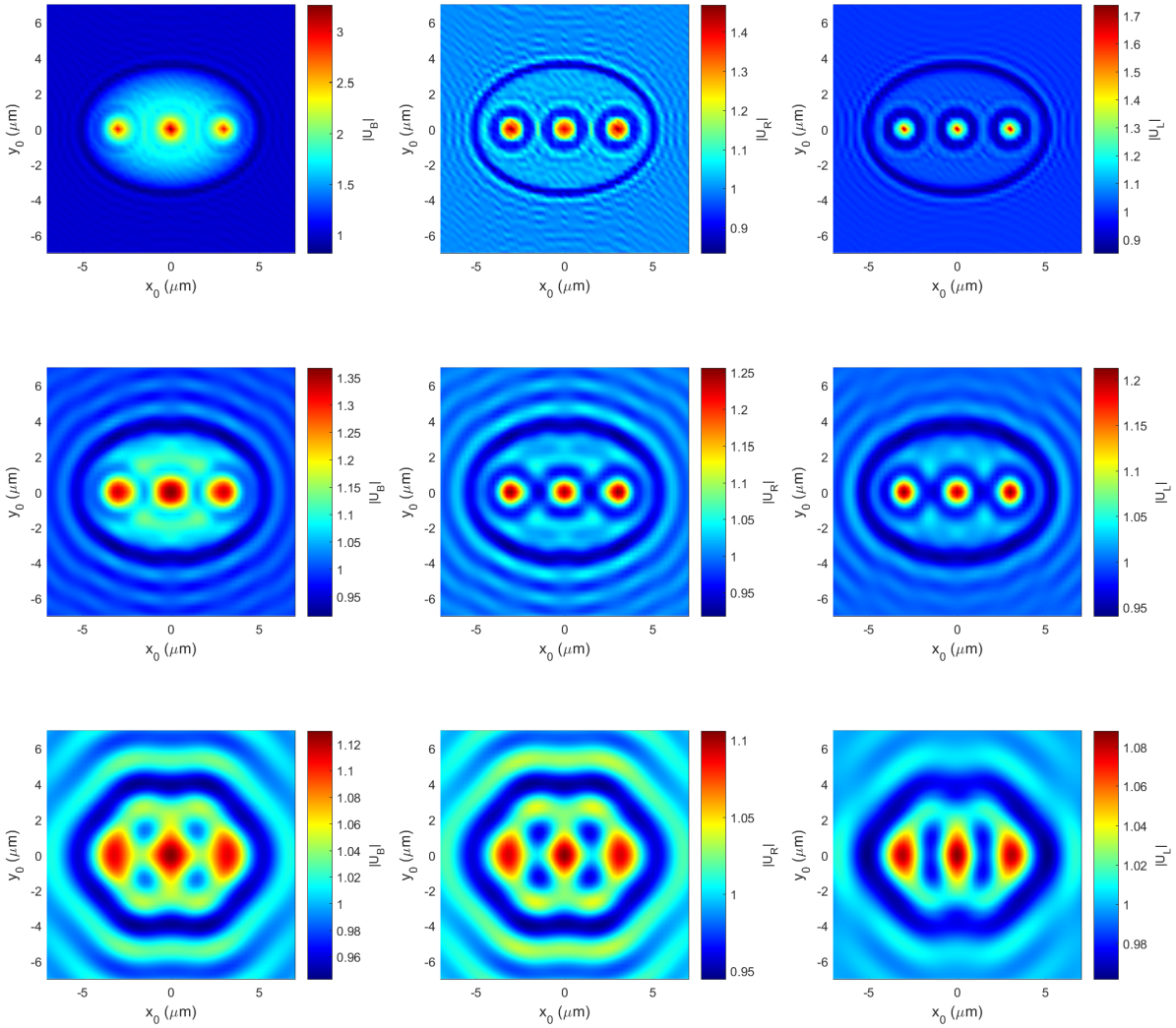

Figure 3.15: Absolute value of total field at distance $z = 150$ nm behind the cell: BA(left), RA(middle), FDTD method(right) for three different wavelengths: 500 nm(up), 1500 nm(middle), 3000 nm(bottom).

4. Simulation of CCHM

4.1 Coherence-Controlled Holographic Microscope

It has been almost 20 years since the first holographic microscope was developed in VUT [38]. Since then, several designs and constructions have been proposed and realized [39, 40]. The last one is coherence-controlled holographic microscope (CCHM) developed in VUT, in co-operation with TESCAN Orsay Holding.

CCHM (Fig. 4.1) is based on computerized off-axis arrangement with special design enabling utilization of spatial and temporal non-coherent illumination. Computerized off-axis arrangement itself enables imaging of transparent, phase objects. It is because the phase shift of the waveform, caused by an object, relative to reference waveform is captured by interference of these two waves. Resulting interference intensity pattern of the object and the reference wave in the image plane can be described as follows

$$i \quad = \quad |u_o + u_r|^2 \quad = \quad |u_o|^2 + |u_r|^2 + u_o^* u_r + u_o u_r^*. \tag{4.1}$$

Complex object wave can be reconstructed by mathematical algorithms. This means, we can extract u_o from the last term of Eq. (4.1) and display its phase and amplitude image.

Optical system is proposed to use Köhler illumination. Here, the light source is imaged to the back focal plane of condenser lens C. This means that each point of the source forms the plane wave in the object space of objective O, and for now, is described by the reduced wave vector $\vec{K} = (\vec{K_t}, K_z) = \vec{k_0}/2\pi$. Specimen plane S is placed in the focal plane of objective O. In the further analysis we consider only the area prompted by the dashed line.

Now, we partially describe theoretical imaging process of CCHM for monochromatic extended source, specifically, imaging of the part mentioned above. The whole description is in [41] and some parts where simulated in [42]. After that, we simulate the object arm of the CCHM, using the previous results, to obtain complex field u_0 behind the aperture diaphragm of objective.

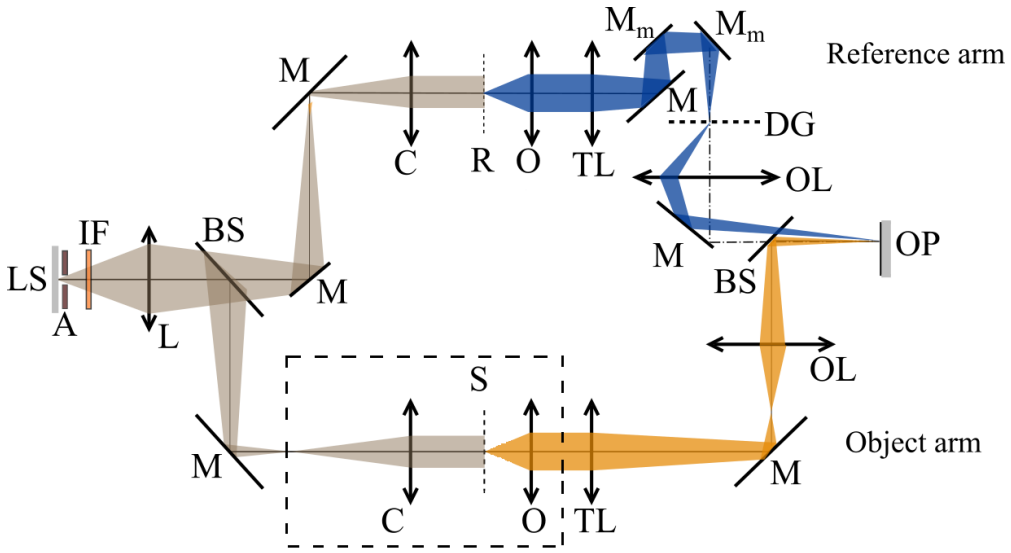

Figure 4.1: Optical set-up of coherence-controlled holographic microscope (CCHM). LS – light source, A – aperture stop of adjustable size, IF – interference filter, L – collector lens, BS – beam splitters, M – mirrors, Mm – movable mirrors, C – condenser lenses, R – reference plane, S – specimen (object) plane, D – diffuser, O – objective lenses, TL – tube lenses, OL – output lenses, DG – diffraction grating, OP – output plane.

4.2 Image formation in CCHM

In many applications in optics, it is useful to express wave in its 2D Fourier spectrum, so-called angular spectrum, i.e. as a superposition of plane waves. It can be shown, that this can be done for any wave satisfying Helmholtz equation [27]. It is usually derived in way, that the whole space is divided by a plane into two subspaces, where one contains all sources of radiation and the other is free space with no sources. In our analysis, we divide the space with the plane perpendicular to propagation axis z, right behind the cell. A wave is then expressed as follows

$$u(\vec{q}) = \iint_{-\infty}^{\infty} U(\vec{K_t}) \exp(2\pi i \vec{K} \cdot \vec{q}) dK_x dK_y, \tag{4.2}$$

where $\vec{q} = (\vec{q_t},z) = (x,y,z)$ is a position vector in a Cartesian coordinate system and $U(\vec{K_t})$ is angular spectrum

$$U(\vec{K_t}) = K^2 \iint_{-\infty}^{\infty} u(\vec{q}) \exp(-2\pi i \vec{K} \cdot \vec{q}) dq_x dq_y. \tag{4.3}$$

Green's function expressed in Sec. 2.4 also satisfy Helmholtz equation at any point except the origin, in other words, outside the cell. This is why we divided our space in such a way. Now we can express spherical wave in angular spectrum [43]

$$\frac{\exp(ik|\vec{q}-\vec{r}'|)}{|\vec{q}-\vec{r}'|} = iK \iint_{-\infty}^{\infty} \exp(2\pi i \vec{K}' \cdot (\vec{q}-\vec{r}')) dK_x' dK_y', \tag{4.4}$$

where

$$\begin{aligned} K_z^{'} &= \sqrt{1 - K_x^{'2} + K_y^{'2}} \quad \text{when} \quad K_x^{'2} + K_y^{'2} \leq K' \\ &= i\sqrt{K' - K_x^{'2} + K_y^{'2}} \quad \text{when} \quad K_x^{'2} + K_y^{'2} > K'. \end{aligned} \tag{4.5}$$

Inserting (4.4) into (2.29) and after some algebraic manipulations, including interchanging the order of integrations and neglecting incident wave, we get

$$U^s(\vec{q}) = \iint_{-\infty}^{\infty} U(\vec{K_t'}; \vec{K_t}) \exp(2\pi i \vec{K'} \cdot \vec{q}) d^2 K_t' \tag{4.6}$$

where

$$U(\vec{K_t'}; \vec{K_t}) = 2\pi \frac{iK^2}{K_z} \iiint_{-\infty}^{\infty} F(\vec{r}',\omega) \exp[2\pi i(\vec{K} - \vec{K}') \cdot \vec{r}'] d^3 r' \sim f_0(\vec{s}_0,\vec{s};\omega), \tag{4.7}$$

where we take only real part of $K_z^{'}$. We see that Fourier coefficients, i.e. field at the infinity, can be obtained by knowing the scattered field $U^s(\vec{q})$ at any distance behind the object. Taking inverse Fourier transform we have

$$U(\vec{K_t'}; \vec{K_t}) = \iint_{-\infty}^{\infty} U^s(\vec{q}) \exp(2\pi i \vec{K'} \cdot \vec{q}) d^2 K_t' \tag{4.8}$$

Thus, for sufficient amount of values $U(\vec{K_t'}; \vec{K_t})$, it could be possible to determine a distribution $F(\vec{r}',\omega)$ of object. This is true within the Born approximation and it is known as the basic theorem of diffraction tomography. It does not have to be sufficiently accurate for some objects.

To physically obtain Fourier spectrum, one have to image the plane waves. This can be achieved by a lens. Then frequency spectrum is imaged at the back focal plane of the objective. This allows us to filter such a frequency spectrum. Filtration is achieved by setting the numerical aperture NA of a condenser and numerical aperture NA_s of an objective. Numerical aperture of rotationally symmetrical system is described by pupil function

$$P(\vec{K_t}) = circ\left(K_t \frac{\lambda_v}{NA}\right), \qquad circ(x) = \begin{cases} 1 & \text{for } x < 1 \\ 1/2 & \text{for } x = 1 \\ 0 & \text{otherwise.} \end{cases} \tag{4.9}$$

Let be $P_C(\vec{K_t})$ and $P_O(\vec{K_t})$ pupil function of condenser, for a flat broad source, and objective respectively. Then the angular spectrum at the back focal plane of condenser is

$$U(\vec{K_t}) = \sqrt{i(\vec{K_t})} P_C(\vec{K_t}), \tag{4.10}$$

where $\sqrt{i(\vec{K_t})}$ is amplitude of frequency spectrum. Setting to unity

$$U(\vec{K_t}) = P_C(\vec{K_t}) \tag{4.11}$$

Then for the complex field u_o at point $\vec{q_t}$ in the image plane of objective, we have

$$u_o(\vec{q_t}) = \int\!\!\int_{-\infty}^{\infty} \int\!\!\int_{-\infty}^{\infty} P_O(\vec{K_t'})[U(\vec{K_t'};\vec{K_t}) + \delta(\vec{K_t'})]P_C(\vec{K_t}) \times \exp(2\pi i \vec{K_t'} \cdot \vec{q_t}) d^2K_t' d^2K_t. \tag{4.12}$$

In Eq. (4.12), $U(\vec{K_t'};\vec{K_t})$ is the Fourier spectrum of scattered field obtained from the results of particular methods at distance $z = 150$ nm and $\delta(\vec{K_t'})$ is Dirac distribution representing contribution from incident wave. The whole simulation is schematically shown in the figure below.

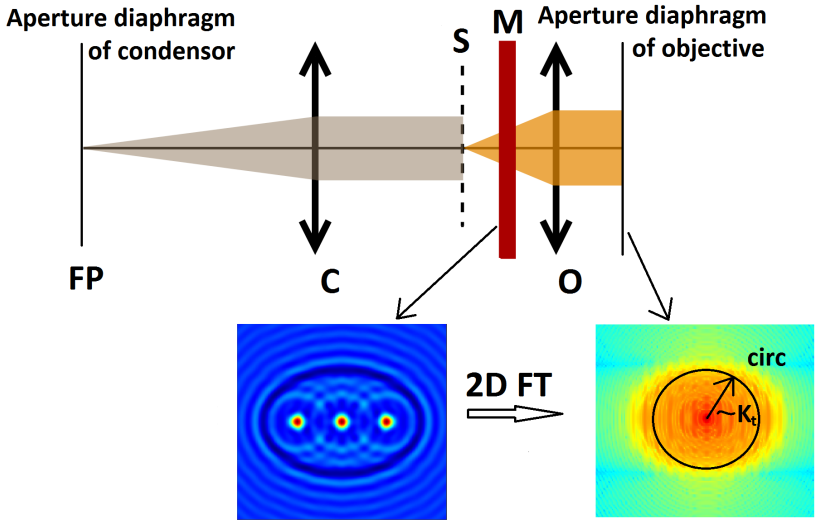

Figure 4.2: Schematic illustration of microscope simulation for Köhler illumination. FP - fourier plane, C - condenser, S - specimen plane, M - monitor, O - objective.

5. Simulation and Results

There are two main goals of simulation, the first is to realize how the resulting signal is affected by setting up various combinations of numerical aperture NA of condenser and numerical aperture NA_s of objective, where $NA \geq NA_s$ must hold. The second one is comparison of signals $u_o(\vec{q_t})$ obtained from the fields U from the BA, RA and FDTD method. Simulations were done in home-made Matlab software.

First, similar as in previous results, we compare 2D Fourier transform for fields $U_{B,R,L}$ obtained at the distance 150 nm behind the cell. We can see results for the particular methods at the top of the Fig. (5.1). Here, the red dot is contribution from incident wave. The incident wave was of the maximal angle ($q = 26$, $p = 13$). At the bottom, we have two slices, one for normal incidence and second for maximal angle passing through maximal value. Here, x-component of transverse wave vector $\vec{K_t}$ were transformed to angle as each value of far-field has its own direction. It is quite hard to tell which method fits better, but from the details we can see, that RA slice trace FDTD better.

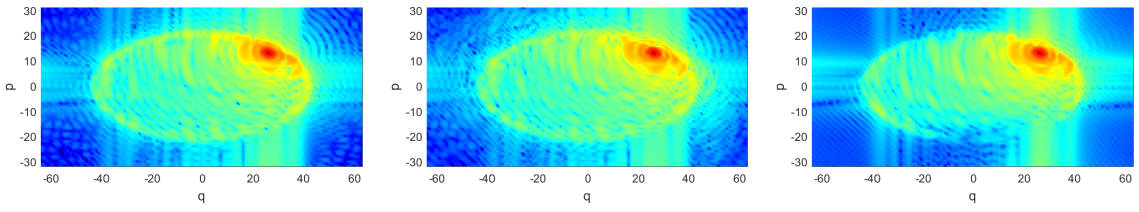

(a) BA (b) RA (c) FDTD

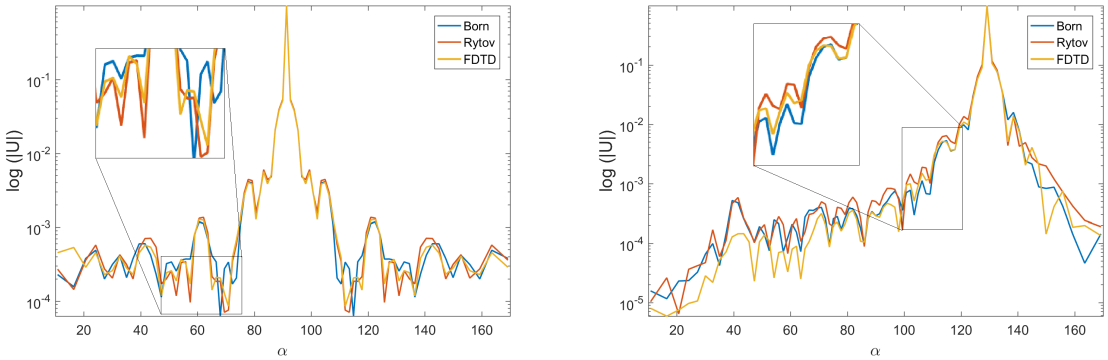

(d) $q = 0$, $p = 0$ (e) $q = 26$, $p = 13$

Figure 5.1: Top: far-field of $U_{B,R,L}$, $q = 26$, $p = 13$; Bottom: slices for two incident waves.

We will now discuss the results from simulation of the object arm. As we stated earlier, cell belongs to phase objects, thus it is the phase of $u_o(\vec{q_t})$ in our interest. In the Fig. (5.2), there are resulting images of simulation for numerical apertures $NA = 0.8$, $NA_s = 0.5$. Visually, the RA looks more similar to the FDTD method than the BA. More detail insight show slices in the Fig. (5.3). It shows values for numerical aperture $NA = 0.4$, $NA_s = 0.1$. These are the first values of numerical aperture for which we can distinguish particular organelles. From the yellow curve representing error, it can be clearly seen, that also here the Rytov method is more accurate. In the next Fig. (5.4), we can see the development of the curve for the numerical aperture of

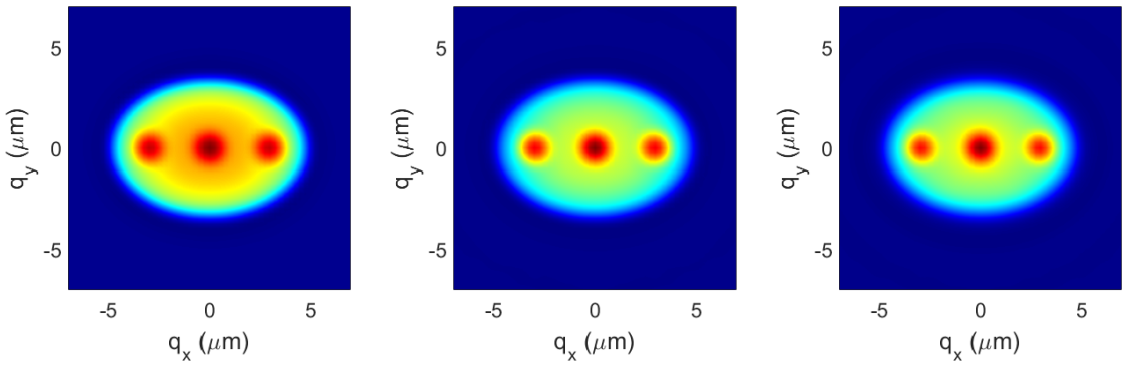

(a) Born (b) Rytov (c) FDTD

Figure 5.2: The phase of the signal u_0 for $NA = 0.8, NA_s = 0.5$

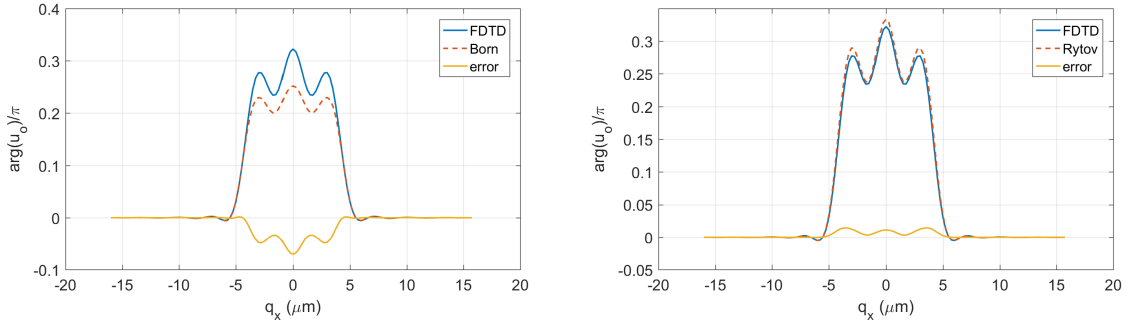

(a) Born/FDTD (b) Rytov/FDTD

Figure 5.3: Slices through the maximal phase values of the signal u_0 for $NA = 0.4, NA_s = 0.1$

condenser $NA = 0.5$ by changing the numerical aperture of objective. Here it can be seen that for $NA_s = 0.1$ there are higher differences between local maximal and minimal values of the peaks compared to previous case. It is clear, that the higher sampling(NA) the better resolution occurs. Even numerical apertures $NA = 0.8$ and $NA_s = 0.1$ displayed in the Fig. (5.5), confirm this. On the other hand the development of curves shows, that for higher values of NA_s the contrast always decreases. Also it can be seen, that for $NA = NA_s$ results do not agree as for $NA > NA_s$.

To conclude the results, we saw that the Rytov approximation is overall more accurate than the Born. As was shown in the chapter of the Rytov approximation, the Born approximation is composed only of first two terms of the Rytov exponential. This confirms, that it is crucial for optically thick and phase object. Even microscope simulation shows that scattered fields obtained from the Rytov approximation provide signal highly accurate to gain signal u_o very similar to the one obtained by the FDTD method. This makes the Rytov method applicable in the inverse scattering methods for such objects, where obtained signal u_0 is processed by reverse algorithm to obtain distribution of the index of refraction. Even BA gives good results and for some usage can be sufficient.

The simulation shows, that for this arrangement of microscope, optimal setup of numerical apertures is to have the highest possible value of NA and NA_s approximately in range $0.1 < NA < 0.2$, for structure of such dimensions. Enhancement of contrast in image can lead to better image processing, for instance setting up threshold. In reality this could lead to low signal and overall worse imaging.

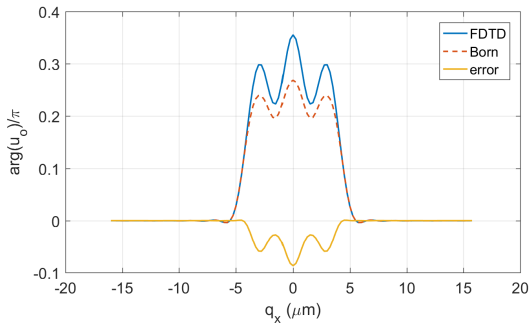

(a) $NA = 0.5, NA_s = 0.1$

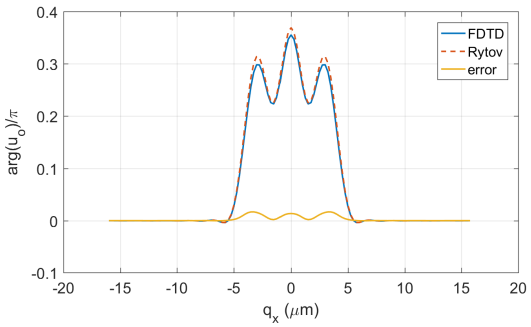

(b) $NA = 0.5, NA_s = 0.1$

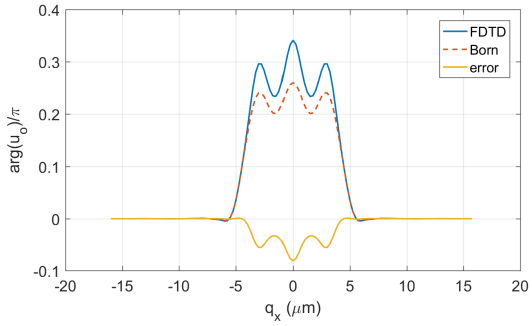

(c) $NA = 0.5, NA_s = 0.3$

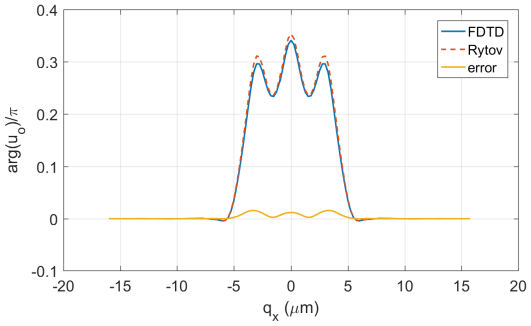

(d) $NA = 0.5, NA_s = 0.3$

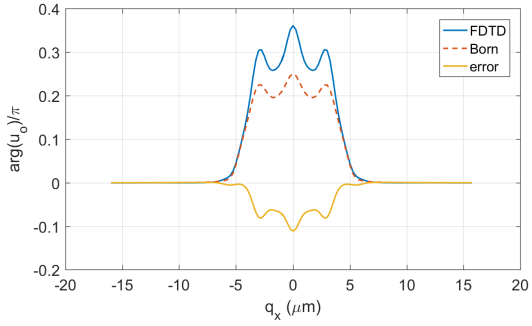

(e) $NA = 0.5, NA_s = 0.5$

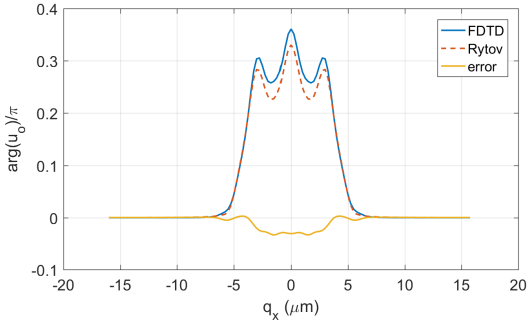

(f) $NA = 0.5, NA_s = 0.5$

Figure 5.4: Slices through the maximal phase values of the signal u_0 for various values of numerical apertures NA_s.

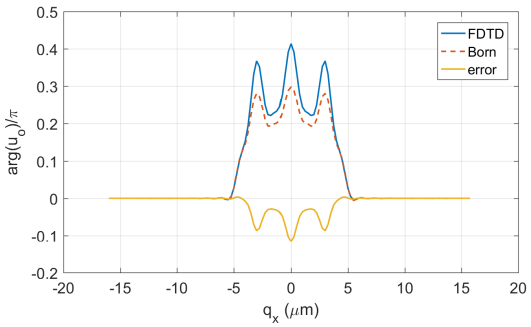

(a) $NA = 0.8, NA_s = 0.1$

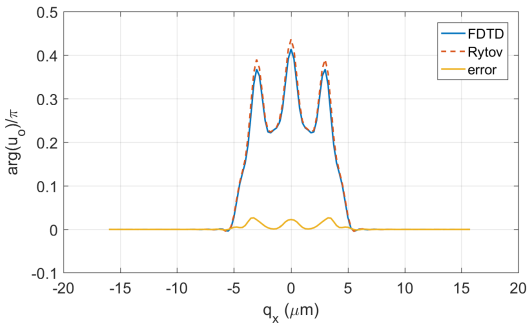

(b) $NA = 0.8, NA_s = 0.1$

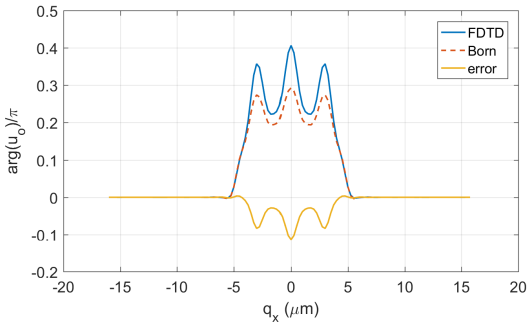

(c) $NA = 0.8, NA_s = 0.3$

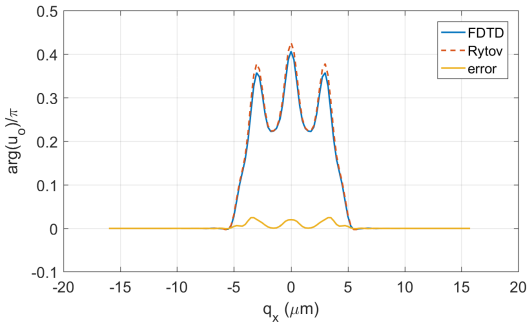

(d) $NA = 0.8, NA_s = 0.3$

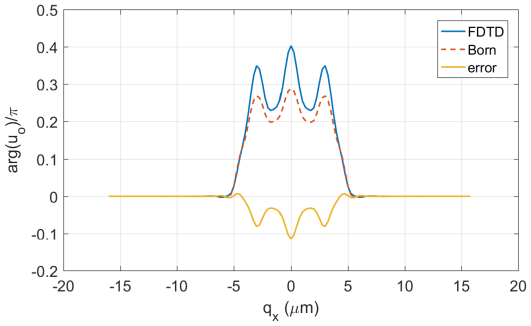

(e) $NA = 0.8, NA_s = 0.5$

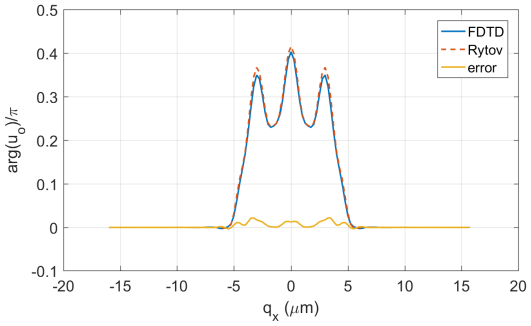

(f) $NA = 0.8, NA_s = 0.5$

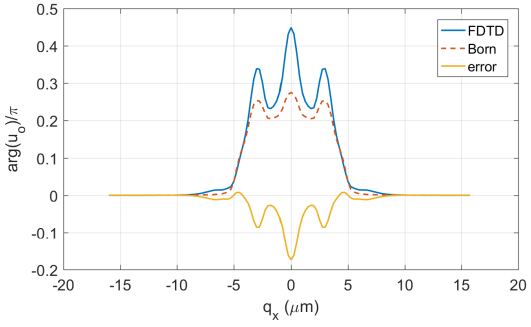

(g) $NA = 0.8, NA_s = 0.8$

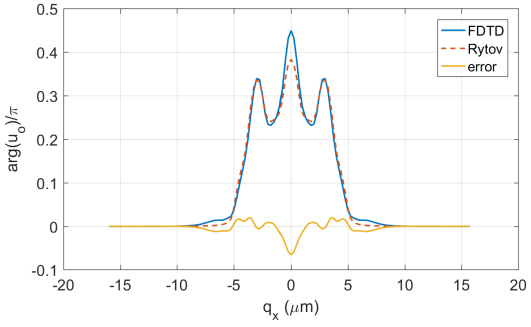

(h) $NA = 0.8, NA_s = 0.8$

Figure 5.5: Slices through the maximal phase values of the signal u_0 for various values of numerical apertures NA_s.

6. Conclusion

The first chapter of the work deals with the research study of the topic. There were introduced several approximative methods dealing with the scattering on biological specimens. Also, several rigorous methods were introduced. The Born method and the Rytov method were chosen as approximative methods. The FDTD method was proposed as rigorous method.

In the second chapter, all three methods were mathematically described. The scattering phase object was introduced. It was the cell consisting of mitochondrion with spherical shape containing three equal organelles uniformly distributed in space.

The approximative scattering on the cell was simulated in home-made Matlab software. The rigorous scattering on the cell was simulated in Lumerical FDTD solutions. The simulations were done for incident plane waves with various angles steps, equidistantly spaced, to imitate Köhler illumination. Approximative methods were compared to the rigorous FDTD method. The results shows that for such object as cell of dimension several micrometers determined by index of refraction n, the Rytov method is notably overall more accurate than the Born method. The Rytov method also shows high accuracy to FDTD method even for high angles. Following analysis showed the fact, that Rytov method is more accurate for optically thick scatterers. On the other hand absolute value of scattered field for optically dense object appears to be better in case of the Born method. It seems, that for some objects, combination of the BA and the RA would fits better.

In the last chapters, the coherence-controlled holographic microscope developed in VUT was introduced. There was shortly reminded mathematical description of object arm for a flat broad coherent source. By the description and the results from the third chapter the resulting signal u_o was simulated for particular methods. The simulation had 2 variable parameters: numerical aperture of condenser NA and numerical aperture of objective NA_s. The results for all methods show the best values of numerical aperture to ensure the highest contrast of resulting signal. The higher numerical aperture NA of condenser the better contrast is obtained. For numerical aperture of objective it is the range $0.1 < NA < 0.2$. Comparison of resulting signal for particular approximative method with FDTD method shows great agreement for both, Rytov method and Born method. But Rytov method gives more accurate results. This makes the Rytov method more applicable in inverse scattering problems.

Bibliography

[1] RAJADHYAKSHA, M.; GROSSMAN, M.; ESTEROWITZ, D.; et al.: In vivo confocal scanning laser microscopy of human skin: melanin provides strong contrast. 1995, doi:10.1111/1523-1747.ep12606215.

[2] SATTLER, E.; KÄSTLE, R.; WELZEL, J.: Optical coherence tomography in dermatology. *Journal of Biomedical Optics*, volume 18, nr. 6, 2013: page 061224, ISSN 1083-3668, doi:10.1117/1.JBO.18.6.061224.

[3] BOAS, D. A.; BROOKS, D. H.; MILLER, E. L.; et al.: Imaging the body with diffuse optical tomography. *IEEE Signal Processing Magazine*, volume 18, nr. 6, 2001: p. 57–75, ISSN 10535888, doi:10.1109/79.962278.

[4] ROGERS, J. D.; RADOSEVICH, A. J.; YI, J.; et al.: Modeling Light Scattering in Tissue as Continuous Random Media Using a Versatile Refractive Index Correlation Function. *IEEE Journal of Selected Topics in Quantum Electronics*, volume 20, nr. 2, 2014: p. 173–186, ISSN 1077-260X, doi:10.1109/JSTQE.2013.2280999.

[5] http://physics.fme.vutbr.cz/~komrska/Difrakce/KapD02.pdf.

[6] LELLI, L.: Aerosol and Clouds WS2014 - Scattering Regimes. 2014.

[7] SI, K.; GONG, W.; SHEPPARD, C. J. R.: Model for light scattering in biological tissue and cells based on random rough nonspherical particles. *Applied Optics*, volume 48, nr. 6, 2009: page 1153, ISSN 0003-6935, doi:10.1364/AO.48.001153.

[8] YULIA, M. SEREBRENNIKOVA ; LUIS, H. G.-R.: Modeling and interpretation of extinction spectra of oriented nonspherical composite particles: application to biological cells.

[9] MISHCHENKO, M. I.; DLUGACH, J. M.; YURKIN, M. A.; et al.: First-principles modeling of electromagnetic scattering by discrete and discretely heterogeneous random media. 2016, doi:10.1016/j.physrep.2016.04.002, <1605.06452>.

[10] NILSSON, A. M. K.; ALSHOLM, P.; KARLSSON, A.; et al.: T-matrix computations of light scattering by red blood cells. *Applied Optics*, volume 37, nr. 13, 1998: page 2735, ISSN 0003-6935, doi:10.1364/AO.37.002735.

[11] PURCELL, E. P. C.: Scattering and adsorption of light by nonspherical dielectric grains. , nr. 186, 1973: p. 705–714.

[12] YURKIN, M. A.; HOEKSTRA, A. G.: The discrete dipole approximation: An overview and recent developments. *Journal of Quantitative Spectroscopy and Radiative Transfer*, volume 106, nr. 1-3, 2007: p. 558–589, ISSN 00224073, doi:10.1016/j.jqsrt.2007.01.034, <0704.0038>.

[13] KARLSSON, A.; HE, J. H. J.; SWARTLING, J.; et al.: Numerical simulations of light scattering by red blood cells. *IEEE Transactions on Biomedical Engineering*, volume 52, nr. 1, 2005: p. 13–18, ISSN 00189294, doi:10.1109/TBME.2004.839634.

[14] YURKIN, M. A.; MALTSEV, V. P.; HOEKSTRA, A. G.: The discrete dipole approximation for simulation of light scattering by particles much larger than the wavelength. *Journal of Quantitative Spectroscopy and Radiative Transfer*, volume 106, nr. 1-3, 2007: p. 546–557, ISSN 00224073, doi:10.1016/j.jqsrt.2007.01.033, <0704.0037>.

[15] BORN, M.; WOLF, E.: *Principles of optics: Electromagnetic Theory of Propagation, Interference and Diffraction of Light*. 1994, ISBN 0521642221, 1–952 p., doi:10.1016/S0030-3992(00)00061-X, <arXiv:1011.1669v3>.

[16] LIM, J.; DING, H. F.; MIR, M.; et al.: Born approximation model for light scattering by red blood cells. *Biomedical Optics Express*, volume 2, nr. 10, 2011: p. 2784–2791.

[17] ISHIMARU, A.: *Wave propagation and scattering in random media*. 1997, ISBN 0780334094, 600 p., doi:10.1016/0034-4257(79)90036-1.

[18] MÜLLER, P.; SCHÜRMANN, M.; GUCK, J.: The Theory of Diffraction Tomography. 2015, ISSN 0031-899X, doi:10.1103/PhysRev.68.142, <1507.00466>.

[19] DEVANEY, A. J.: Inverse-scattering theory within the Rytov approximation. *Optics letters*, volume 6, nr. 8, 1981: p. 374–376, ISSN 0146-9592, doi:10.1364/OL.6.000374.

[20] WAX, A.; BACKMAN, V.: *Biomedical applications of light scattering*. McGraw Hill, 2010.

[21] RUDOLPH, W.; KEMPE, M.: Trends in optical biomedical imaging. 1997, doi:10.1080/09500349708230763.

[22] ZERNIKE, F.: Phase contrast, a new method for the microscopic observation of transparent objects. *Physica*, volume 9, nr. 7, 1942: p. 686–698, ISSN 00318914, doi:10.1016/S0031-8914(42)80035-X.

[23] HOFFMAN, R.; GROSS, L.: Modulation Contrast Microscope. *Applied Optics*, volume 14, nr. 5, 1975: page 1169, ISSN 0003-6935, doi:10.1364/AO.14.001169.

[24] www.tescan.com.

[25] GOODMAN, J. W.: *Introduction to Fourier Optics McGraw-Hill Series in Electrical and Computer Engineering*, volume 8. 1996, ISBN 0974707724, 491 p., doi:10.1088/1355-5111/8/5/014, <0070242542>.

[26] KAZUMI WATANABE: *Integral transform techniques for Green's function.* Springer Cham Heidelberg New York Dordrecht London, 2015, ISBN 978-3-319-00878-3, doi:10.1007/978-3-319-00879-0.

[27] KOMRSKA, J.: *The Fourier methods in diffraction theory in optics and in structure analysis.* Brno 2007: CERM.

[28] TATARSKI, V. I.: *Wave Propagation in a Random Medium (McGraw-Hill, New York, 1961).*

[29] TAFLOVE, A.; HAGNESS, S. C.: *Computational Electrodynamics: The Finite-Difference Time-Domain Method, Third Edition.* 2005, ISBN 978-1-58053-832-9, 1038 p., doi:10.1515/9783110809824.v.

[30] THOMAS, V. A.; PIKET-MAY, M.; TAFLOVE, A.; et al.: The Use of SPICE Lumped Circuits as Sub-grid Models for FDTD Analysis. *IEEE Microwave and Guided Wave Letters*, volume 4, nr. 5, 1994: p. 141–143, ISSN 10518207, doi:10.1109/75.289516.

[31] KARLSSON, A.; HE, J.; SWARTLING, J.; et al.: Numerical simulations of light scattering by red blood cells. *IEEE Transactions on Biomedical Engineering*, volume 52, nr. 1, 2005: p. 13–18, ISSN 00189294, doi:10.1109/TBME.2004.839634.

[32] YEE, K.: Numerical solution of initial boundary value problems involving Maxwell's equations in isotropic media. 1966, doi:10.1109/TAP.1966.1138693.

[33] INAN, U. S.; MARSHALL, R. A.: *Numerical electromagnetics: The FDTD method*, volume 9780521190. 2011, ISBN 9780511921353, 1–390 p., doi:10.1017/CBO9780511921353.

[34] GEDNEY, S. D.: Introduction to the Finite-Difference Time-Domain (FDTD) Method for Electromagnetics. *Synthesis Lectures on Computational Electromagnetics*, volume 6, nr. 1, 2011: p. 1–250, ISSN 1932-1252, doi:10.2200/S00316ED1V01Y201012CEM027.

[35] www.lumerical.com.

[36] BÉRENGER, J.-P.: Perfectly Matched Layer (PML) for Computational Electromagnetics. *Synthesis Lectures on Computational Electromagnetics*, volume 2, nr. 1, 2007: p. 1–117, ISSN 1932-1252, doi:10.2200/S00030ED1V01Y200605CEM008.

[37] ZIEGEL, E.; PRESS, W.; FLANNERY, B.; et al.: Numerical Recipes: The Art of Scientific Computing. *Technometrics*, volume 29, nr. 4, 1987: page 501, ISSN 00401706, doi:10.2307/1269484, <arXiv:1011.1669v3>.

[38] CHMELÍK, R.; HARNA, Z.: Parallel-Mode Confocal Microscopy. *Optical Engineering*, volume 38, nr. 10, 1999: p. 1635–1639.

[39] KOLMAN, P.; CHMELÍK, R.: Coherence-controlled holographic microscope. *Optics Express*, volume 18, nr. 21, 2010: page 21990, ISSN 1094-4087, doi:10.1364/OE.18.021990.

[40] SLABÝ, T.: New generation coherence-controlled holographic microscope. *Brno: University of Technology, Faculty of Mechanical Engineering*, 2014: page 91.

[41] CHMELIK, R.; SLABA, M.; KOLLAROVA, V.; et al.: The Role of Coherence in Image Formation in Holographic Microscopy. *Progress in Optics*, volume 59, 2014: p. 267–335, ISSN 00796638, doi:10.1016/B978-0-444-63379-8.00005-2.

[42] HENZLOVA, M.: Theoretical description of imaging by a digital holographic microscope. *Brno: University of Technology, Faculty of Mechanical Engineering*, 2010.

[43] MANDEL, L.: *Optical Coherence and Quantum Optics*, volume 64. 1996, ISBN 0521417112, 1438 p., doi:10.1119/1.18450.

List of Tables